

A thermodynamic metric quantitatively predicts disordered protein partitioning and multicomponent phase behavior

Zhuang Liu,^{1,*} Beijia Yuan,^{1,2,3,*} Mihir Rao,^{1,3} Gautam Reddy,³ and William M. Jacobs^{1,†}

¹*Department of Chemistry, Princeton University, Princeton, NJ 08544, USA*

²*Lewis-Sigler Institute for Integrative Genomics, Princeton University, Princeton, NJ 08544, USA*

³*Department of Physics, Princeton University, Princeton, NJ 08544, USA*

(Dated: March 10, 2026)

Intrinsically disordered regions (IDRs) of proteins mediate sequence-specific interactions underlying diverse cellular processes, including the formation of biomolecular condensates. Although IDRs strongly influence condensate compositions, quantitative frameworks that predict and explain their phase behavior in complex mixtures remain lacking. Here we introduce a thermodynamic model that quantitatively predicts the behavior of arbitrary combinations of IDRs across a wide range of concentrations, with accuracy comparable to state-of-the-art simulations. The model learns low-dimensional, context-independent representations of IDR sequences that combine to form mixture representations, producing context-dependent interactions. These representations define a thermodynamic metric space in which distances between IDRs correspond directly to differences in their thermodynamic properties. We show that the model predicts multicomponent phase diagrams in quantitative agreement with molecular simulations without being trained on free-energy or phase-coexistence data. The metric space provides geometrically intuitive predictions of IDR partitioning, multicomponent condensation, and context-dependent mutational effects, addressing several central problems in IDR biophysics within a single model. Systematic interrogation of the learned representations reveals how amino-acid composition and sequence patterning jointly determine mixture thermodynamics. Together, our results establish a unified and interpretable framework for predicting and understanding the behavior of complex mixtures of IDRs and other sequence-dependent biomolecules.

I. INTRODUCTION

Sequence-specific interactions among intrinsically disordered regions (IDRs) underlie cellular processes including transcriptional regulation, signaling, and the formation of biomolecular condensates.^{1–5} Individual IDRs exhibit selective partitioning behavior, enriching in some condensates while being excluded from others.^{6–9} Subtle sequence differences can strongly influence IDR interaction specificity.^{10–16} However, because IDR interactions emerge from conformational heterogeneity and depend on mixture composition, they are inherently context dependent and difficult to predict. There is currently no unifying thermodynamic description of sequence-encoded specificity that achieves quantitative accuracy in multicomponent environments characteristic of cells.

Various sequence-based approaches have addressed aspects of this problem, but treat them in isolation. Machine-learning models have been trained to classify single-component phase-separation propensity, predict co-phase separation in binary mixtures, or categorize sequences by their partitioning behavior in selected condensates, but this classification paradigm limits predictions to predefined categories and cannot generalize to arbitrary mixtures.^{14,17–23} “Grammar”-oriented models have provided mechanistic insights into sequence properties that drive condensation within specific protein fam-

ilies; however, these models are context-specific and do not extend to arbitrary combinations of IDRs without fine-tuning.^{24–28} More fundamentally, these approaches are not formulated in terms of general thermodynamic principles, limiting generalization across mixtures and leaving the molecular origins of interaction specificity unresolved.

Physics-based simulations provide a general and physically grounded description of sequence-dependent IDR thermodynamics.^{29,30} Coarse-grained simulations can now reproduce conformational statistics of individual IDRs^{31,32} and show promising agreement with experimentally determined phase diagrams.^{33–35} However, the computational cost of phase-coexistence simulations precludes systematic exploration of sequence space and mixture composition, limiting investigation of partitioning specificity to case studies.³⁶ Mean-field approaches and polymer-physics theories^{37–41} have therefore been developed to predict IDR interactions analytically, but existing multicomponent formulations assume pairwise additivity,^{42–44} an approximation that is generally valid only at dilute concentrations.⁴⁵ No general approach exists to systematically improve such models toward simulation-level accuracy while retaining interpretability.

Here we introduce a unified model that quantitatively predicts context-dependent IDR interactions from sequences and concentrations. By expressing interaction specificity as distances between thermodynamic functions, the model subsumes many existing classification problems and enables quantitative prediction of partitioning specificity, multicomponent condensation, and

* Authors contributed equally

† wjacobs@princeton.edu

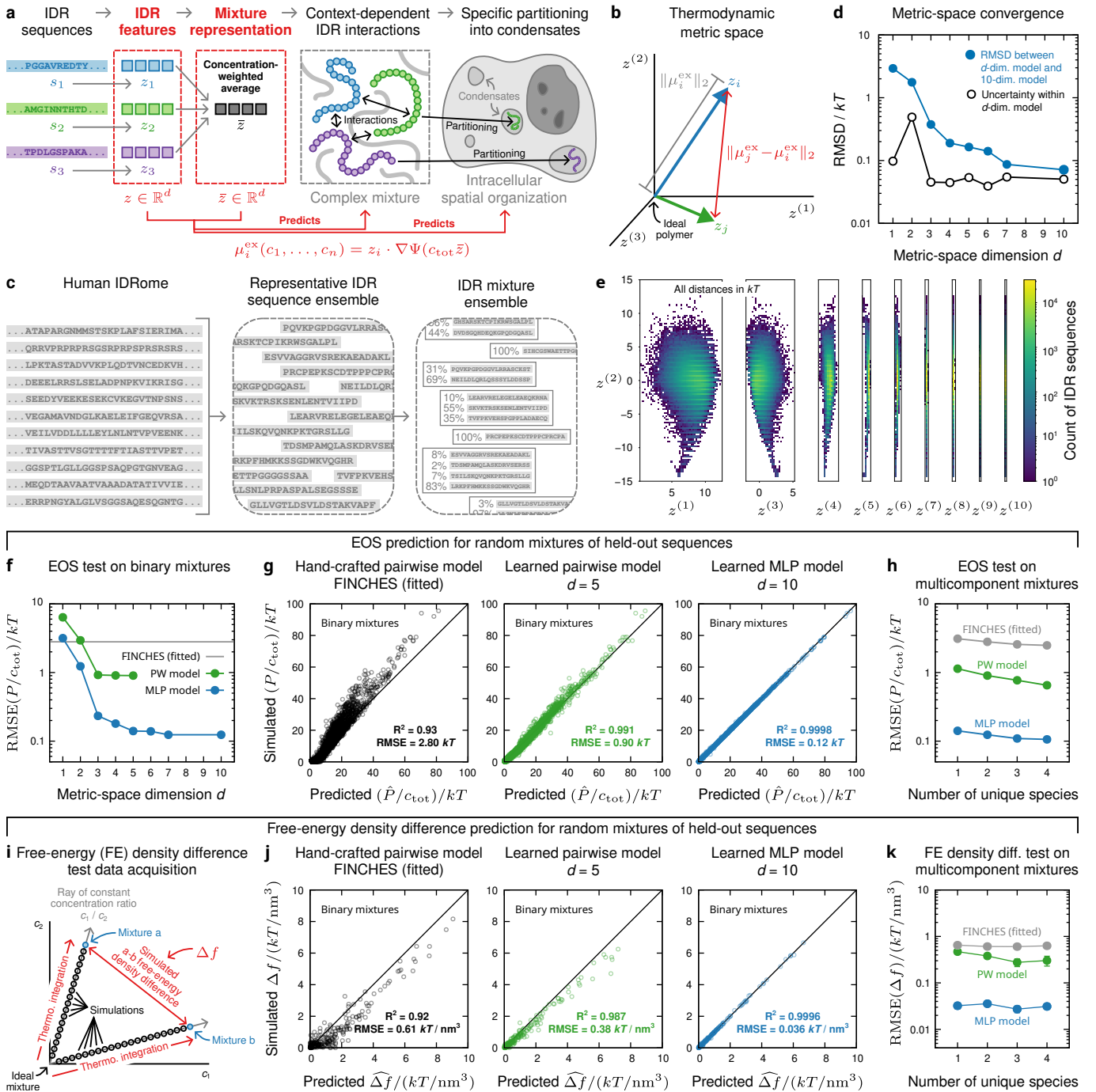


FIG. 1. An interpretable thermodynamic model quantitatively predicts IDR interactions in multicomponent mixtures. (a) Context-independent IDR feature vectors combine in a concentration-weighted average to define a mixture representation; these d -dimensional vectors predict context-dependent IDR interactions via the excess chemical potential function μ^{ex} . (b) IDR feature vectors reside in a thermodynamic metric space in which distances correspond to a norm of the difference between μ^{ex} functions. This space is uniquely determined by the mixture ensemble. (c) We curated training and test IDRs by fragmenting the human IDRome into equal-length sequences of 20 residues. This produced an ensemble of 335,439 minimally overlapping representative fragments, which were combined into mixtures by sampling from a mixture ensemble. (d) Convergence of the MLP-model metric space with increasing dimension d . (e) Two-dimensional projections of feature vectors in the $d = 10$ MLP-model metric space, with distances in units of kT . Histograms show the distribution of all fragments in the sequence ensemble. (f) EOS test performance, $\text{RMSE}(P/c_{\text{tot}})$, on 10,440 random binary mixtures as a function of the metric-space dimension d and (g) corresponding scatter plots for three models: FINCHES⁴⁴ with fitting parameters chosen by training on EOS data, a learned pairwise model with $d = 5$, and the MLP model with $d = 10$. (h) EOS test performance on random n -component mixtures for the same three models. (i) A test set of 231 free-energy density differences, Δf , between random binary mixtures was constructed by performing explicit thermodynamic integration. (j) Scatter plots showing test performance on the FE test set for the three models considered in (g). (k) FE test performance, $\text{RMSE}(\Delta f)$, on random n -component mixtures for the same three models. Error bars indicate the standard deviation over random mixture pairings. In (f–k), sequences that compose the random mixtures were sampled uniformly from the metric space of the $d = 10$ MLP model.

context-dependent mutational effects within a common framework. In this framework, sequences are represented as vectors in a *thermodynamic metric space* sufficient to determine IDR behavior across mixture compositions. This representation provides a physically interpretable coordinate system for interrogating the sequence determinants of IDR interactions and establishes a general thermodynamic geometry for sequence-dependent interactions in complex mixtures.

II. RESULTS AND DISCUSSION

A. A thermodynamic metric for sequence space

We hypothesized that the thermodynamic behavior of IDRs in multicomponent mixtures is governed by a small number of sequence features.⁴⁶ Here we identify and interpret these features using a symmetry-preserving machine-learning framework trained on high-throughput simulations.

We first introduce a general framework that is provably sufficient to describe arbitrary mixture thermodynamics. We represent each IDR sequence by a d -dimensional *feature vector*, z (Fig. 1a). Crucially for interpretability, these feature vectors contain all information required to predict an IDR’s thermodynamic behavior in arbitrary mixtures and are thus context-independent. Feature vectors combine via a concentration-weighted average to produce a *mixture representation*, \bar{z} . This mixing rule implies that the excess chemical potential function of IDR i , which describes the contribution of IDR i to the free energy of an n -component mixture, is equal to

$$\mu_i^{\text{ex}}(c_1, \dots, c_n) = z_i \cdot \nabla \Psi(c_{\text{tot}} \bar{z}), \quad (1)$$

where c_1, \dots, c_n are the concentrations of IDRs in the mixture, c_{tot} is the total concentration, and $\nabla \Psi$ is the gradient of the learned excess free-energy density (see Methods). Eq. (1) expresses a simple interaction rule: context-dependent interactions arise from the alignment between a sequence feature vector and the gradient of the mixture free-energy landscape.

Quantifying differences in the thermodynamic behaviors of IDRs requires comparisons across mixture environments. Such comparisons are meaningful only relative to a “prior” distribution of mixtures, which specifies the thermodynamic contexts that can be encountered. We therefore choose a physically meaningful coordinate system for the feature vectors by defining a μ^{ex} function (L_2) norm over this prior (see Methods),

$$\|z_j - z_i\| = \|\mu_i^{\text{ex}} - \mu_j^{\text{ex}}\|_2. \quad (2)$$

In this *thermodynamic metric space*, Euclidean distances between feature vectors equal L_2 distances between their excess chemical potential functions (Fig. 1b). Thus, two IDRs are close if and only if they behave similarly across mixtures drawn from the prior, independent of sequence

similarity. For a fixed prior, the metric space is unique up to orthogonal transformations about the origin, which corresponds to an ideal polymer. We orient the space using principal component analysis of $\|\mu^{\text{ex}}\|$.

To define thermodynamic environments of biological interest, we constructed a statistically diverse sequence ensemble and mixture prior. We fragmented the human IDRome into minimally overlapping segments of fixed length (20 residues), yielding 335,439 representative fragments (Fig. 1c). This controls for leading-order polymer-length effects, allowing us to focus on sequence-dependent interactions;¹⁵ however, the framework can be straightforwardly generalized to variable-length sequences. We then constructed a mixture ensemble by uniformly sampling sequences and biasing mole fractions toward mixtures strongly enriched in only a few components, as is typical of condensates (see Methods). This mixture prior defines the thermodynamic environments over which distances and specificity are evaluated.

To test our hypothesis that IDR mixture thermodynamics is governed by a small number of sequence features, we applied our framework to a state-of-the-art coarse-grained force field (Mpipi) that recapitulates experimentally observed behaviors across diverse IDR chemistries.³⁵ Because Mpipi is sequence-specific and not tuned to a particular protein family or condensate type, it provides a suitable platform for uncovering broadly applicable sequence features. We therefore used this force field to train an implementation of our framework using an encoder–decoder architecture; we refer to this implementation as the MLP model (see Methods). Rather than performing explicit free-energy or phase-coexistence calculations, we trained the model solely on equation-of-state (EOS) data from inexpensive simulations (see Methods and Fig. S1). We then systematically varied d to discover the dimensionality of the metric space.

We find that the thermodynamic behavior of IDR mixtures, as described by Mpipi, is intrinsically low dimensional: at most $d \approx 10$ dimensions are required to resolve differences in excess chemical potential functions across the mixture prior to $\lesssim 0.1 kT$ accuracy (Fig. 1d). Moreover, the first few dimensions account for most of the variance of feature vectors across the IDR sequence ensemble (Fig. 1e). This compact representation enables quantitative prediction of free energies, chemical potentials, and phase behavior in arbitrary mixtures without additional simulation.

B. Quantitative prediction of multicomponent mixture thermodynamics

If the thermodynamic metric space accurately encodes excess chemical potentials, it should quantitatively reproduce EOS data and free energies for mixtures not seen during training. We therefore evaluated model predictions on mixtures composed exclusively of held-out IDRs. For the $d = 10$ MLP model, EOS predictions are

in quantitative agreement with simulations of random binary mixtures sampled uniformly from the metric space (Fig. 1f; see also Fig. S2). Errors decrease rapidly with increasing dimensionality and saturate near $d \approx 10$, mirroring convergence of the metric-space structure (Fig. 1d).

To isolate the roles of model expressivity and feature dimensionality, we compare against two alternatives (see also Fig. S3). The first is a learned pairwise (PW) model that restricts sequence-specific information to a quadratic function of concentrations, as in the Flory–Huggins (FH) theory.⁴⁵ Despite being trained on the same data, the reduced expressivity of the PW model collapses the representation to $d \approx 3$ thermodynamically meaningful dimensions. This indicates that the PW approximation captures coarser sequence features relative to the MLP model. Nonetheless, the learned PW model achieves lower errors than FINCHES,⁴⁴ a recently proposed pairwise model based on hand-crafted interaction rules within the FH framework. To make this second comparison, we adjusted global parameters for the FINCHES interaction and length scales to minimize EOS root-mean-square error (RMSE; see Extended Methods). All three models show strong correlations between predicted and simulated pressures (Fig. 1g); however, only the learned models achieve quantitative accuracy below the thermal energy of $1 kT$.

Model performance improves as the number of distinct components in random mixtures increases from one to four (Fig. 1h). This improvement reflects self-averaging in multicomponent systems, consistent with the linear mixing structure of the metric space. Component-level variability partially averages out, enabling scalable and robust predictions without additional assumptions.

Although the model was trained on EOS data, thermodynamic behavior is governed by the free-energy landscape. To assess whether the model accurately predicts free energies, we constructed a test set of 231 free-energy density differences between random binary mixtures by performing explicit thermodynamic integration of simulation data (Fig. 1i). Free-energy accuracy mirrors EOS accuracy overall (Fig. 1j). The MLP model accurately reconstructs the underlying free-energy landscape, while pairwise models incur substantial errors, especially when based on hand-crafted interaction rules. Free-energy accuracy remains stable with increasing component number (Fig. 1k), demonstrating that the learned representation scales naturally to arbitrary mixtures.

C. Quantitative prediction of multicomponent phase diagrams

Having established that the model accurately predicts free-energy density differences, we next examined whether it captures the resulting phase behavior. Because phase coexistence is determined by the global structure of the free-energy landscape,^{47–50} it provides a stringent test of whether the thermodynamic metric space

captures collective behavior in the thermodynamic limit. We therefore asked whether the model can quantitatively predict multicomponent phase diagrams without being trained on explicit examples of phase coexistence.^{47,51}

We first generated binary phase diagrams for representative pairs of IDR sequences sampled uniformly from the metric space (Fig. 2a). For each pair, phase boundaries were computed directly from the predicted free-energy density using a multicomponent common-tangent construction,⁵² without any training on coexistence data. Each predicted phase diagram specifies whether a mixture at a given parent concentration remains homogeneous or phase-separates into coexisting phases connected by tie lines (Fig. 2b).

We validated these predictions using direct-coexistence molecular dynamics simulations. For selected parent concentrations, simulations either remained homogeneous or phase-separated into coexisting phases, in agreement with model predictions (Fig. 2b,c). Whereas direct-coexistence simulations require extensive equilibration, phase diagrams from the free-energy model are obtained essentially instantaneously once the model is learned.

To quantify agreement systematically, we constructed a test set of 59 parent concentrations sampled from the representative phase diagrams in Fig. 2a. For each parent concentration, we compared the predicted phase behavior to the equilibrium distribution of local concentrations measured in a direct-coexistence simulation. Agreement was quantified using the Wasserstein (earth-mover) distance W_1 between predicted thermodynamic-limit concentration distributions and those obtained from finite-size simulations (Fig. 2d). Because direct-coexistence simulations are subject to significant finite-size effects arising from interfacial fluctuations and limited sampling volumes, we benchmarked W_1 against a positive control—the smallest possible distance given the simulated concentration distribution—and a negative control constructed by pairing simulations with random predictions that preserve the parent concentration (Fig. 2e).

Both the learned MLP and PW models perform near the positive control in the vast majority of test cases, indicating quantitative agreement within finite-size uncertainties. Comparable results were obtained for random mixtures assembled from sequences seen (Fig. 2e) or held-out (Fig. S4) during EOS training. Differences between learned models are small relative to finite-size uncertainties in the simulations. By contrast, FINCHES performs comparably to the negative control on these benchmarks.

The strong agreement between predicted and simulated phase behavior demonstrates that the learned feature vectors are sufficient to reproduce multicomponent phase diagrams. Together with EOS and free-energy validation, these results show that the thermodynamic metric space captures sequence-dependent interaction specificity and accurately describes mixtures in the thermodynamic limit. This quantitative foundation enables a direct geometric interpretation of the thermodynamic metric space.

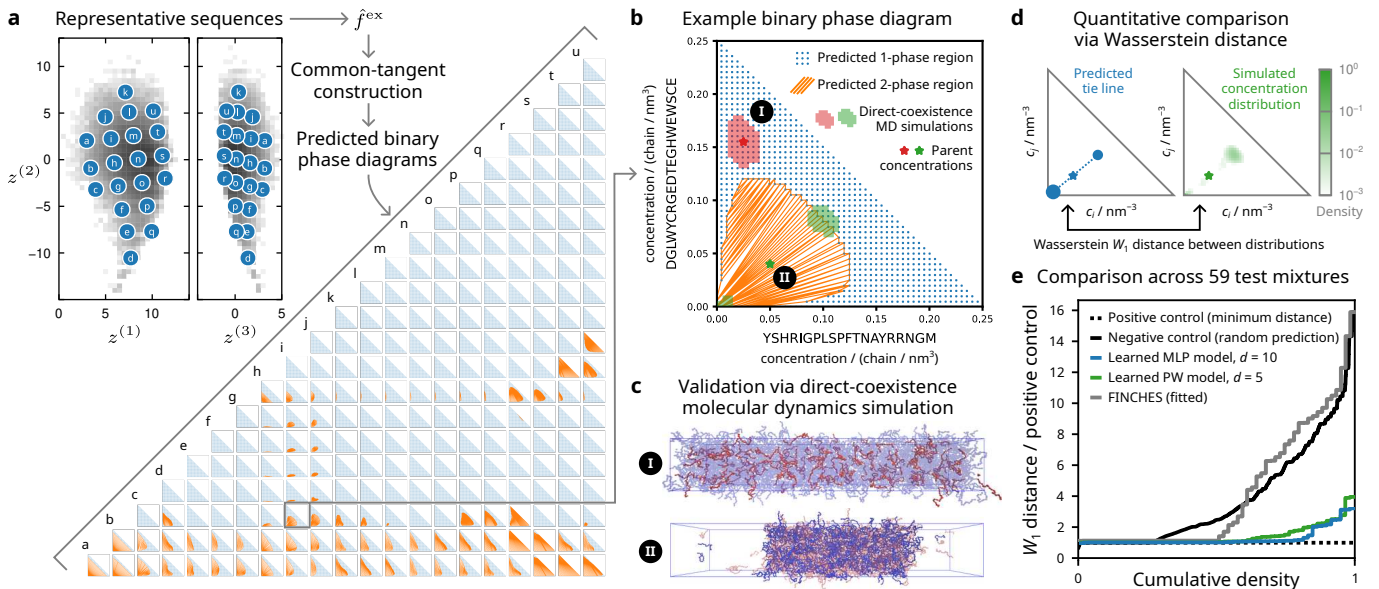


FIG. 2. **The model quantitatively predicts multicomponent IDR phase diagrams.** (a) Using representative sequences sampled uniformly from the metric space, we applied the $d = 10$ MLP model to predict a matrix of binary phase diagrams. (b) In this example phase diagram (for representative sequences c and i), blue points indicate concentrations at which the mixture is predicted to be homogeneous. Orange lines indicate two-phase regions; mixtures with parent concentrations within these regions are predicted to phase-separate into coexisting phases connected by the orange tie lines. (c) Predictions from (b) are compared with direct-coexistence molecular dynamics simulations at two selected parent concentrations, labeled I and II. Equilibrium simulation snapshots indicate that parent concentration I is a homogeneous mixture, whereas parent concentration II phase separates. The distributions of local concentrations observed in simulations are summarized by thresholded histograms (shaded regions) in (b). (d) Comparisons are quantified using the Wasserstein W_1 distance between the predicted one- or two-phase distribution in the thermodynamic limit and the distribution of local concentrations in direct-coexistence simulations at the same parent concentration. (e) The distribution of normalized W_1 distances was computed for a test set of 59 parent concentrations sampled from (a) for the three models considered in Fig. 1f–k. The positive control is the smallest possible W_1 distance for each mixture given the simulated concentration distribution. The negative control was constructed by pairing simulations with random predictions that preserve the parent concentration. Examples from the test set are shown in Fig. S4.

D. Geometric interpretation of partitioning, multicomponent condensation, and mutational effects

The thermodynamic metric space organizes IDRs by their interactions rather than sequence similarity. As a result, interaction specificity can be understood directly from geometric relationships in this space. We illustrate this connection by answering three central questions in IDR thermodynamics: why specific IDRs are recruited into some condensates but excluded from others, why particular combinations of IDRs form droplets, and why the impact of a mutation depends on the ensemble of mixture environments that can be encountered.

Partitioning offers the clearest illustration of this geometric structure. An IDR partitions into a mixture, such as one of the condensates illustrated in Fig. 3a, when its excess chemical potential is negative, $\mu_i^{ex} < 0$, and is excluded when $\mu_i^{ex} > 0$. Since the excess chemical potential is given by an inner product between the feature vector z_i and the gradient of the excess free-energy density, partitioning depends on their alignment evaluated at $c_{tot}\bar{z}$. Because both z and \bar{z} share the same metric

space, partitioning reduces to a geometric classification problem (Fig. 3b–d). For a given IDR of interest, the metric space is divided into regions that either recruit or exclude that IDR as a function of the mixture representation (Fig. 3d). Conversely, for a given mixture of interest, geometric classification identifies IDRs that are either included or excluded from that environment. The thermodynamic geometry therefore provides immediate intuition: an IDR strongly partitions into a mixture when the gradient of the mixture’s excess free-energy density is oppositely aligned with the IDR feature vector.

The same geometric framework also explains multicomponent condensation. Condensation is the formation of an IDR-enriched droplet in coexistence with a dilute solution, whose EOS satisfies $P \approx c_{tot}^{(dil.)} kT \approx 0$ (Fig. 3e).^{47,48} Condensation is predicted to occur if the coexistence equation $P(c_{tot}^{(cond.)}, \bar{z}) \approx 0$ admits a solution for the condensed-phase total concentration, $c_{tot}^{(cond.)} > 0$, at fixed \bar{z} . These solutions define a \bar{z} -dependent condensation region that can be used to classify both single-component and multicomponent mixtures (Fig. 3f). A single-component IDR mixture condenses if its representation $\bar{z} = z$ lies within the condensation region. For mul-

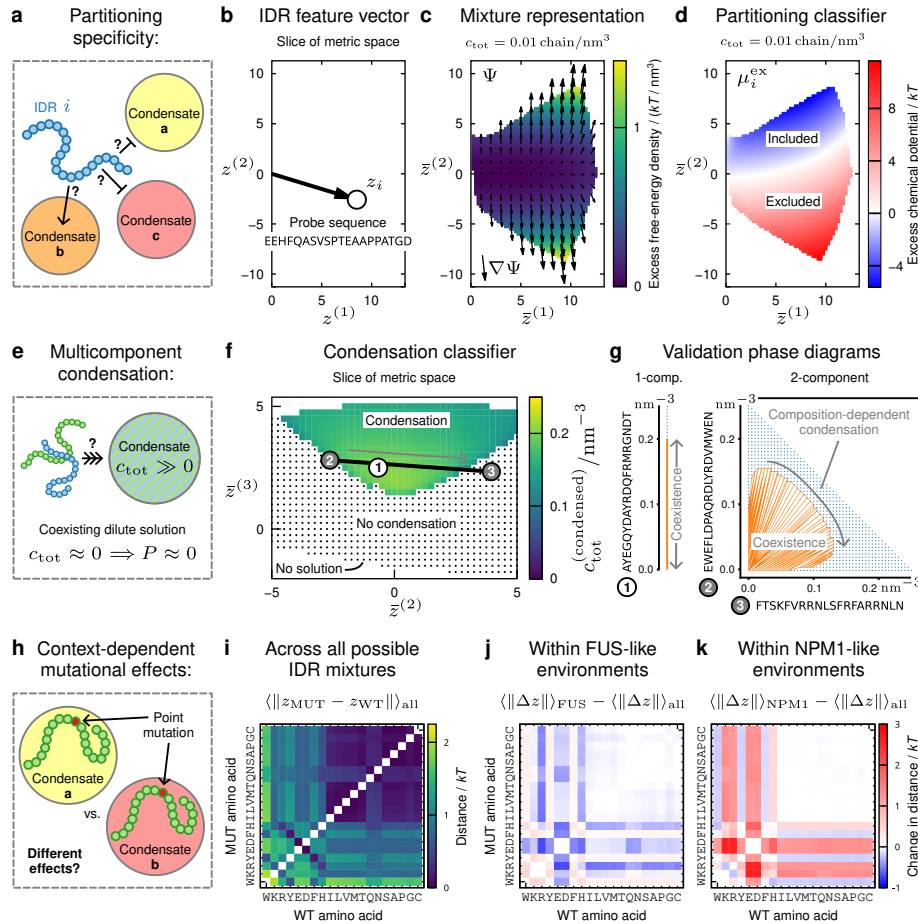


FIG. 3. The thermodynamic metric space organizes IDRs according to their physical interactions. (a) Partitioning specificity refers to the tendency of an IDR to be included in or excluded from condensates with different compositions. This can be predicted directly from the geometry of the metric space, since the excess chemical potential of an IDR is the inner product of (b) the IDR feature vector, z_i , and (c) the gradient of the excess free-energy density, $\nabla\Psi$, evaluated at $c_{\text{tot}}\bar{z}$. (d) This construction yields a classifier for inclusion, $\mu_i^{\text{ex}}(c_{\text{tot}}\bar{z}) < 0$, or exclusion, $\mu_i^{\text{ex}}(c_{\text{tot}}\bar{z}) > 0$, of the probe IDR i in (b) as a function of the mixture representation \bar{z} in (c). For visualization, we plot a two-dimensional slice of the metric space at constant c_{tot} in (c,d). (e) Condensation occurs when a concentrated droplet coexists with a dilute solution. (f) This can be predicted directly within the metric space by looking for solutions to the condensation coexistence equation $P_{\text{coex}} \approx 0$, yielding a classifier for both individual IDRs and IDR mixtures. For visualization, we show a two-dimensional slice of the metric space. The colored region indicates where $P_{\text{coex}} \approx 0$ has a nontrivial solution, leading to a droplet with the indicated c_{tot} . A single IDR condenses if its feature vector lies within this region, whereas an IDR mixture undergoes mole fraction-dependent condensation if the convex hull of its components' feature vectors intersects this region. (g) These predictions are confirmed by unary and binary phase diagrams, respectively, for probe IDR 1 and the pair of probe IDRs 2 and 3 shown in (f); in the binary case, moving along the line segment in (f) corresponds to sweeping through mole fractions from 100% IDR 2 to 100% IDR 3 in (g). (h) The effects of point mutations on IDR interactions depend on the composition of the local environment. (i) The metric space can be exploited to quantify the effects of all single-amino-acid substitutions, $\|\Delta z\| = \|z_{\text{MUT}} - z_{\text{WT}}\|$. These are averaged over the IDR sequence ensemble to obtain a matrix of mean mutation distances. Because this calculation makes use of the uniform prior introduced in Fig. 2a, it reflects mutational effects across all possible IDR mixtures. Amino acids are ordered according to the leading wild-type mode of variation in the mutation-distance matrix, indicating an overall ranking of thermodynamic importance. Specializing the prior to mixtures composed only of (j) FUS fragments, which are relatively hydrophobic, or (k) NPM1 fragments, which are enriched in negative charge, rescales metric distances, revealing context dependence across distinct ensembles of mixture environments. All calculations were performed using the $d = 10$ MLP model.

ticomponent mixtures, condensation occurs if the convex hull of component representations $\{z_1, \dots, z_n\}$ intersects this region, leading to mole fraction-dependent condensation. Unary and binary phase diagrams (Fig. 3g) confirm these predictions for the example IDR sequences whose

feature vectors are indicated in Fig. 3f. Thus, single-component and multicomponent condensation emerge from the same unified classifier in the metric space.

Beyond predicting mixture behavior, the metric structure also quantifies context-dependent mutational effects

(Fig. 3h). The thermodynamic impact of a mutation is determined by the change in μ^{ex} across the mixture prior, which is captured by the Euclidean distance between wild-type (WT) and mutant (MUT) feature vectors, $\|\Delta z\| = \|z_{\text{MUT}} - z_{\text{WT}}\|$. Averaged over the IDR ensemble, this yields a matrix of mean point-mutation distances (Fig. 3i). Substitutions involving aromatic (W, Y, F) and charged (K, R, E, D) residues produce the largest overall perturbations, consistent with the dominant electrostatic, π - π , and cation- π interaction modes encoded in the underlying force field.

Because distances depend on the mixture prior, this framework naturally captures environmental specificity. Restricting the prior to FUS-like mixtures (hydrophobic and weakly positively charged) or to NPM1-like mixtures (polar and strongly negatively charged), as opposed to the uniform prior over all IDR sequences, rescales mutational effects via a linear transformation (Fig. 3j,k; see Methods and Fig. S5). These comparisons reveal that charged residues tend to exhibit the strongest differential effects in like-charged environments. Together, these examples illustrate how the mixture prior enables both global and highly specialized calculations within a single model, without re-training. The metric-space geometry therefore provides a unified and computationally efficient framework for predicting partitioning, condensation, and mutational sensitivity across diverse mixture contexts.

E. Learned feature vectors encode amino-acid composition and sequence patterning

Having used the metric-space geometry to interpret collective behavior, we next asked how the learned coordinates arise from sequence. Because the feature vectors are learned solely by optimizing mixture thermodynamics, they are not constrained by predefined sequence descriptors. We therefore asked whether theoretical descriptors developed for single IDRs^{21,54-57,59,60} are reflected in the learned metric space and to what extent it encodes additional thermodynamic information.

We related theoretical descriptors to the learned feature vectors of the $d = 10$ MLP model using two complementary analyses of the sequence ensemble. Canonical correlation analysis (CCA) identifies the strongest *linear* relationships between theoretical descriptors and the learned coordinates (Fig. 4a). This analysis shows that several theoretical descriptors associated with charge and short-range interactions are strongly aligned with the first few dimensions of the metric space.⁶¹ In particular, net charge is largely captured by a single coordinate, $z^{(2)}$, consistent with the geometric interpretation of partitioning in Fig. 3b-d, where mixtures attract IDRs with oppositely signed $z^{(2)}$. Mutual information analysis⁶², which quantifies *arbitrary nonlinear* dependencies, yields a similar ranking of features but reveals additional structure (Fig. 4b and Fig. S6). As higher dimensions are included, the mutual information I between theoretical

descriptors and metric coordinates continues to increase, in contrast to CCA, indicating nonlinear relationships between theoretical and learned features in these dimensions. Overall, the amino-acid composition descriptor set³⁵ and NARDINI patterning descriptor set⁵³ exhibit substantially higher I than suggested by CCA, implying that the encoding of composition and patterning depends nonlinearly on sequence context.

To assess how well combinations of theoretical descriptors approximate the metric space, we used a greedy procedure to select descriptor subsets that maximize I and compared this to the entropy H of the learned coordinates (Fig. 4c; see Extended Methods). Although theoretical descriptors explain a substantial fraction of the structure, they do not fully account for the learned coordinates, since $I < H$. At the same time, the learned representation is more compact than theoretical descriptor sets, requiring fewer dimensions to capture thermodynamically relevant variability (Fig. S6).

F. Composition-independent sequence patterning effects are captured by the learned metric space

We next asked whether the learned feature vectors accurately describe composition-independent sequence patterning effects.^{11,21,25,53,59,63} This cannot be assessed using WT sequences alone, because no two IDRs in our ensemble share identical amino-acid composition. We therefore sampled composition-preserving mutants by performing residue swaps and scoring candidate sequences with the ESM2 protein language model,⁵⁸ ensuring that mutants were drawn from the same empirical distribution as WT sequences (see Extended Methods).

We performed EOS simulations for mutant mixtures by replacing each WT sequence in the binary-mixture test set with a MUT sequence. Comparison of paired WT and MUT simulations reveals composition-independent EOS differences of $\sim 0.3 kT$ between paired mixtures (Fig. 4d). These effects are substantially smaller than typical point-mutation effects (Fig. 3i), consistent with the dominant role of amino-acid composition in determining thermodynamic behavior across diverse backgrounds.

We then evaluated whether the thermodynamic metric space captures these patterning effects. The predictive accuracy of the $d = 10$ MLP model is comparable for WT and MUT mixtures, indicating generalization to composition-preserving rearrangements. At the same time, the model clearly discriminates WT and MUT mixtures, as evaluating the model with their labels interchanged increases the prediction error to $\sim 0.3 kT$, approximately the maximum signal permitted by the data.

Finally, we examined how this capability depends on dimensionality. Truncating the feature vectors to $d < 10$ progressively reduces the ability to distinguish WT from MUT mixtures, with discrimination largely lost by $d \approx 3$. Lower dimensions therefore encode the dominant compositional determinants of thermodynamics, whereas pat-

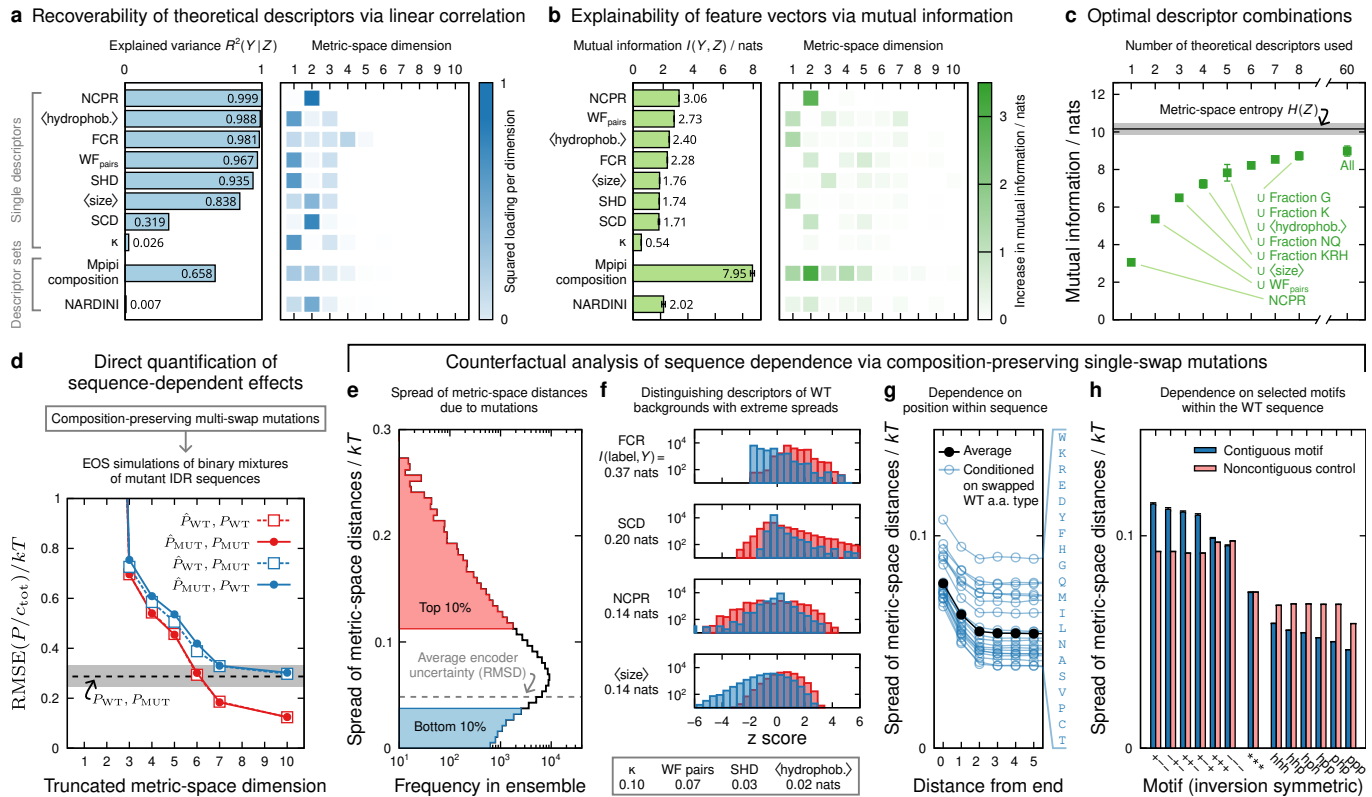


FIG. 4. Systematic interrogation of learned feature vectors quantifies the compositional and sequence-dependent determinants of IDR mixture thermodynamics. (a) The explained variance and corresponding metric-space loading vector, representing the optimal linear projection of theoretical descriptor(s) Y onto learned feature vectors Z , are shown for each of eight individual descriptors, as well as for the 12-element Mpipi compositional descriptor set³⁵ and the associated 40-element NARDINI patterning descriptor set.⁵³ Individual descriptors are net charge per residue (N CPR),⁵⁴ average hydrophobicity,³⁵ fraction of charged residues (FCR),⁵⁴ a mean-field summary of short-ranged interactions (WF_{pairs}),²¹ sequence hydrophobicity decoration (SHD),⁵⁵ average residue size,³⁵ sequence charge decoration (SCD),⁵⁶ and the charge-patterning descriptor κ .⁵⁷ (b) The mutual information $I(Y, Z)$, which quantifies the overall (nonlinear) relationship between Y and Z , is shown along with the increase in $I(Y, Z)$ as each dimension is added to Z . (c) Theoretical descriptor sets that best approximate the metric space, according to greedy maximization of $I(Y, Z)$. The order in which the descriptors are added to the set is indicated; the final point uses all 60 descriptors, including Mpipi composition and NARDINI descriptors. The entropy of the 335,439 IDR feature vectors, $H(Z)$, is shown for comparison (black line and gray region indicating SEM). (d) The magnitude of composition-independent effects was quantified by comparing EOS simulations of mixtures of wild-type (WT) and mutant (MUT) IDR sequences sampled according to ESM2 likelihood;⁵⁸ MUT mixtures were constructed by replacing the WT sequences in the binary-mixture test set (Fig. 1f,g). Red points indicate the test performance on WT and MUT mixtures given by the RMSE between prediction, \hat{P} , and simulation, P . Blue points show the results of swapping the MUT and WT labels when evaluating the model. The root-mean-square difference between paired WT and MUT simulations, $\langle((P_{MUT} - P_{WT})/c_{tot})^2\rangle$, is shown for comparison (black dashed line and gray region indicating SEM). (e) A counterfactual analysis considered all unique single-swap mutants, weighted in accordance with ESM2 likelihood, around each WT sequence. The histogram shows the distribution of the spread (RMSD of feature vectors relative to the centroid in the metric space) of these mutants around each of the 100,000 WT sequences in the test set. (f) The distributions of selected theoretical descriptors for WT sequences with extreme spreads, lying in the bottom (B, blue) or top (T, red) 10% of the spreads shown in (e). The ability of each of the 8 individual theoretical descriptors to predict the label T or B of an extreme WT sequence is quantified by the mutual information $I(\text{label}, Y)$. (g) The average spread conditioned on the distance of the swapped positions from the end of the sequence and the WT amino acids at the swapped positions; higher values indicate that counterfactuals satisfying these criteria result in larger perturbations on average. (h) The average spread conditioned on whether the swapped positions affect a contiguous or non-contiguous motif within the WT sequence. Results are presented for motifs consisting of triplets of charged (+ or -), hydrophobic/polar (h or p), or, as a control, all (*) amino acids. All calculations were performed using the $d = 10$ MLP model. Error bars, if shown, indicate SEM; otherwise, errors are smaller than the symbol sizes.

tering effects reside in higher dimensions. This inter-pretation is consistent with the strongest association between compositional features and the first few dimensions of the feature vectors (Fig. 4b), which also account for the greatest variance across the IDR ensemble (Fig. 1e).

G. A systematic analysis reveals when and how patterning matters

To determine when and how residue order matters beyond composition, we performed an analysis of all unique single-swap mutants for each of the 100,000 WT sequences in the test set. These counterfactual variants are minimal perturbations that preserve amino-acid composition. For each WT background, we quantified sensitivity to residue order by computing the spread of mutation distances, defined as the root-mean-square deviation (RMSD) of WT and MUT feature vectors about their centroid and weighted by ESM2 likelihood.

Across this ensemble, swap-induced spreads typically exceed feature-vector uncertainty (Fig. 4e). However, the magnitude of these effects varies substantially among WT backgrounds. To identify sequence properties associated with heightened sensitivity, we compared sequences in the top and bottom 10% of the spread distribution. We examined theoretical descriptor distributions for these two classes and quantified their informativeness using mutual information (Fig. 4f). Charge-related features are most predictive, led by the fraction of charged residues (FCR), which tends to be greater for high-sensitivity WT backgrounds.^{11,59} By contrast, hydrophobicity-related features show similar distributions across the two classes.

We then used the counterfactual analysis to identify patterning effects not fully described by existing theoretical descriptors. Two qualitative effects emerge clearly. First, the model exhibits an absolute positional dependence along the chain. Conditioning on swap position shows that mutations within two to three residues of either chain end produce substantially larger perturbations to feature vectors on average (Fig. 4g). Stratification by amino-acid identity further reveals that strongly interacting residues (W, K, R, E, D, Y, F) generate the largest effects when located near chain ends. This behavior is physically intuitive: strongly interacting residues can form more intermolecular contacts when positioned near an end than when buried in the chain interior.

Second, we analyzed linear motifs defined as contiguous triplets of charged (+ or -) or hydrophobic/polar (h/p) residues. For each motif class, we computed the average spread for swaps affecting such motifs and compared these to controls in which the same residue types were distributed throughout the sequence. Charged and hydrophobic motifs exhibit distinct behaviors (Fig. 4h): rearrangements that alter adjacency between oppositely charged residues produce larger perturbations than controls, whereas clustered hydrophobic residues reduce the

effect of swapping relative to controls.²⁵ However, mutations affecting like-charged blocks resemble controls, indicating that adjacency of opposite charges is the dominant effect uncovered by this motif analysis. Together, these observations demonstrate that the thermodynamic metric representation resolves composition-dependent sequence-patterning determinants of IDR behavior in complex mixtures.

III. CONCLUSIONS

We show that the thermodynamic behavior of intrinsically disordered proteins in complex mixtures is low dimensional and can be captured by a compact metric representation. Sequence-dependent interaction specificity is encoded by the geometry of the thermodynamic metric space, enabling quantitative prediction of chemical potentials, mixture free energies, and multicomponent phase behavior directly from sequences.

This framework is interpretable in two complementary senses. From the perspective of sequence-based prediction, each IDR is assigned a context-independent feature vector determined by its amino-acid composition and sequence patterning, and mixture properties follow from a simple linear combination of these feature vectors. From the sequence-agnostic perspective of thermodynamic geometry, distances in the metric space correspond directly to differences in excess chemical potentials across mixtures of interest. Together, these views unify prediction of partitioning specificity, single- and multicomponent condensation, and mutational sensitivity within a single physical framework.

Our results clarify several central aspects of IDR thermodynamics. The collective behavior of IDRs in multicomponent mixtures, including context-dependent interactions, emerges from a small number of sequence features. Pairwise models can achieve partial accuracy when coefficients are learned, but they restrict the sequence information available for thermodynamic prediction. The influence of sequence patterning on mixture thermodynamics depends on amino-acid composition: patterning effects appear in higher dimensions of the metric space and are modulated by dominant compositional features encoded in lower dimensions.

Although the present implementation inherits limitations of the underlying force field, the framework provides a practical route for systematic refinement. Because it is trained directly on thermodynamic observables, it can incorporate multicomponent experimental data and simulations at mixed resolution. Rather than reducing interaction specificity to a set of classification problems, our thermodynamic metric approach derives specificity directly from the mixture free-energy landscape within a unified physical framework. In doing so, it establishes a general, interpretable foundation for quantitatively predicting multicomponent, sequence-dependent phase behavior in biological and synthetic heteropolymers.

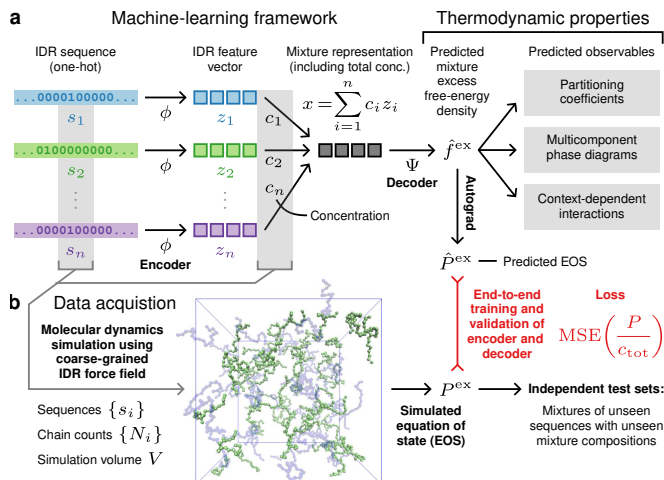


FIG. 5. **Symmetry-preserving framework for predicting mixture free energies.** (a) Our custom machine-learning framework consists of an encoder ϕ , which maps each sequence to its feature vector, and a decoder Ψ , which predicts the excess free-energy density, \hat{f}^{ex} , from the mixture representation. Equilibrium thermodynamic properties are then obtained from \hat{f}^{ex} . (b) We trained the model by performing coarse-grained molecular dynamics simulations^{35,64} of random IDR mixtures and minimizing the loss between the predicted, \hat{P} , and simulated, P , EOS. Simulations of mixtures of held-out sequences were used to construct independent test sets.

ACKNOWLEDGMENTS

This work is supported by the National Institute of General Medical Sciences of the National Institutes of Health under award number R35GM155017 to WMJ.

IV. METHODS

A. A symmetry-preserving thermodynamic model for IDR mixtures

We formulate IDR interactions at the level of mixture thermodynamics by predicting the free-energy density of a mixture as a function of sequence and concentration. Once this quantity is known, all equilibrium thermodynamic observables—including the equation of state, chemical potentials, and phase behavior—follow by differentiation. This formulation treats IDR interactions as emergent properties of the mixture rather than reducing them to pairwise affinities or abstract weights in classification models.

Our machine-learning framework consists of an encoder–decoder architecture designed to respect the fundamental symmetries of mixture free energies (Fig. 5a). The encoder ϕ maps each IDR sequence to a context-independent feature vector $z \in \mathbb{R}^d$. The mixture representation $\bar{z} \in \mathbb{R}^d$ is a concentration-weighted average of the feature vectors of its components, so that

contextual effects arise solely from how features combine in mixtures. The decoder Ψ predicts the excess free-energy density relative to an ideal mixture, \hat{f}^{ex} , from the decoder input $x = c_{\text{tot}}\bar{z}$. This formulation naturally enforces extensivity and permutation invariance,⁶⁵ yielding the following simple and general form for the excess free-energy density of an n -component mixture,

$$z_i = \phi(\text{sequence}_i), \quad x = \sum_{j=1}^n c_j z_j, \quad \hat{f}^{\text{ex}} = \Psi(x), \quad (3)$$

with boundary conditions $\Psi(0) = \nabla\Psi(0) = 0$ that recover ideal-mixture behavior at vanishing concentration. We implement the encoder using a transformer architecture to capture sequence dependence and the decoder using a multilayer perceptron (MLP). Details are provided in the Extended Methods.

This formulation is provably sufficient in the limit of large dimension d (see Extended Methods). Importantly, by learning from thermodynamic observables, a model with fixed d acquires a representation optimized for mixture thermodynamics rather than predefined sequence descriptors.

B. Learning free energies from equations of state

Free energies are not direct observables in molecular simulations. Rather, they are typically obtained through thermodynamic integration, which is computationally expensive, or via direct simulations of phase coexistence, which are sensitive to equilibration and finite-size effects.⁶⁶ To circumvent this limitation, we trained the model on a thermodynamic derivative that is directly accessible: the excess contribution to the equation of state (EOS), P^{ex} , defined as the deviation of the pressure from ideal-mixture behavior. The excess pressure can be computed straightforwardly from standard molecular dynamics simulations in the canonical (NVT) ensemble. Unlike phase-coexistence calculations, which may or may not show phase separation, each EOS simulation yields a well-defined pressure measurement so that all simulations contribute information during training. The predicted excess pressure, \hat{P}^{ex} , is obtained by automatic differentiation of the learned free-energy density,

$$\hat{P}^{\text{ex}} = x \cdot \nabla\Psi(x) - \Psi(x), \quad (4)$$

ensuring thermodynamic consistency by construction. We therefore trained the model by minimizing the mean-squared-error (MSE) of $P^{\text{ex}}/c_{\text{tot}}$, which results in consistent simulation uncertainties across concentrations. As in conventional thermodynamic integration, this EOS training strategy allows the use of simulations comprising a relatively small number of chains without incurring substantial finite-size effects. Moreover, sampling thermodynamically unstable mixtures does not compromise

training, because the model learns a globally defined free-energy function with which unstable regions can be self-consistently diagnosed.

We applied this framework to the Mpipi force field, a coarse-grained description of intrinsically disordered proteins.³⁵ IDR fragments were divided into training, validation, and test sets, with test mixtures constructed exclusively from held-out sequences. Training data were generated from simulations of random unary and binary mixtures of IDR fragments (Fig. 5b). The model was trained end-to-end, jointly learning the sequence encoder and mixture decoder so that similarities among IDR sequences could be exploited to reduce data requirements. See the Extended Methods for further details.

C. Defining the thermodynamic metric space

The excess chemical potential of IDR fragment i is obtained by differentiating the learned excess free-energy density, $\hat{\mu}_i^{\text{ex}} = \partial \hat{f}^{\text{ex}} / \partial c_i$, yielding Eq. (1); in the main text, we have suppressed the $\hat{\cdot}$ notation, which indicates that this is a prediction, for legibility. Eq. (1) makes explicit that the thermodynamic properties of an IDR in an arbitrary mixture are determined by the alignment of its feature vector with the local gradient of the excess free-energy function, regardless of whether IDR i has nonzero concentration in the mixture.

We define thermodynamic distances using the $L_2(\rho_{\text{mix}})$ norm of $\hat{\mu}_i^{\text{ex}}$ over a prior distribution of mixtures ρ_{mix} . We parameterize mixtures by total concentration c_{tot} and mole fractions c_i/c_{tot} , and assume a factorized prior $\rho_{\text{mix}}(c) = p(c_{\text{tot}})p(c/c_{\text{tot}})$. We take c_{tot} to be uniform on $(0, 0.25 \text{ chain/nm}^3]$. In the large- n limit this yields sparse mixtures with an average effective cardinality (99% mass) of 2.5, emphasizing environments enriched in only a few (typically 1–10 nonzero) components while sampling all

possible sequence combinations.

We independently trained $K = 5$ models using 5-fold cross-validation, yielding learned latent vectors $\{z_i^{(k)}\}$ and a corresponding decoder $\tilde{\Psi}^{(k)}$ for each trained model $k = 1, \dots, K$. Following from Eq. (1), the mixture prior induces a positive semidefinite matrix for each model k ,

$$M^{(k)} = \int d\tilde{x} \rho_{\text{mix}}(\tilde{x}) \nabla \tilde{\Psi}^{(k)}(\tilde{x}) \nabla \tilde{\Psi}^{(k)}(\tilde{x})^\top, \quad (5)$$

which we estimate by Monte Carlo sampling from ρ_{mix} . The squared $L_2(\rho_{\text{mix}})$ norm of $\hat{\mu}_i^{\text{ex}}$ is therefore $\tilde{z}_i^{(k)} M^{(k)} (\tilde{z}_i^{(k)})^\top$, defining an inner product on latent space. Defining $A^{(k)} = (M^{(k)})^{1/2}$ as the principal matrix square root yields the linear transformation

$$z_i^{(k)} = \tilde{z}_i^{(k)} (A^{(k)})^\top, \quad (6)$$

so that Euclidean distances in the transformed coordinates reproduce the $\hat{\mu}_i^{\text{ex}}$ norm. Importantly, because Eq. (6) is linear, the mixture prior can be changed to redefine distances without retraining the model, as demonstrated in Fig. 3j,k. This procedure converts each learned latent space into a consistent thermodynamic metric space in which distances satisfy Eq. (2), with a corresponding transformed decoder $\Psi^{(k)}$.

After applying the metric transformation, we canonicalize each of the K models by uncentered principal component analysis, fixing axis orientations by a consistent sign convention. This procedure aligns the K models in a common coordinate system. We report the model-averaged z_i after canonicalization as the feature vector for IDR i and quantify encoder uncertainty by the RMSD across the K models. The final result is a thermodynamic metric space in which Euclidean distances correspond to differences in excess chemical potentials across mixtures drawn from the specified prior.

-
- [1] A. S. Holehouse and B. B. Kragelund, *Nat. Rev. Mol. Cell Biol.* **25**, 187 (2024).
 - [2] C. P. Brangwynne, C. R. Eckmann, D. S. Courson, A. Rybarska, C. Hoegge, J. Gharakhani, F. Jülicher, and A. A. Hyman, *Science* **324**, 1729 (2009).
 - [3] C. P. Brangwynne, P. Tompa, and R. V. Pappu, *Nat. Phys.* **11**, 899 (2015).
 - [4] M. Feric, N. Vaidya, T. S. Harmon, D. M. Mitrea, L. Zhu, T. M. Richardson, R. W. Kriwacki, R. V. Pappu, and C. P. Brangwynne, *Cell* **165**, 1686 (2016).
 - [5] Y. Shin and C. P. Brangwynne, *Science* **357**, eaaf4382 (2017).
 - [6] S. F. Banani, H. O. Lee, A. A. Hyman, and M. K. Rosen, *Nat. Rev. Mol. Cell Bio.* **18**, 285 (2017).
 - [7] J. A. Ditlev, L. B. Case, and M. K. Rosen, *J. Mol. Biol.* **430**, 4666 (2018).
 - [8] A. S. Holehouse and S. Alberti, *Mol. Cell* **85**, 290 (2025).
 - [9] B. R. Sabari, A. A. Hyman, and D. Hnisz, *Nat. Rev. Genetics* **26**, 279 (2025).
 - [10] Y.-H. Lin, J. D. Forman-Kay, and H. S. Chan, *Phys. Rev. Lett.* **117**, 178101 (2016).
 - [11] H. Lyons, R. T. Veettil, P. Pradhan, C. Fornero, N. De La Cruz, K. Ito, M. Eppert, R. G. Roeder, and B. R. Sabari, *Cell* **186**, 327 (2023).
 - [12] N. De La Cruz, P. Pradhan, R. T. Veettil, B. A. Conti, M. Oppikofer, and B. R. Sabari, *Mol. Cell* **84**, 3497 (2024).
 - [13] T. Agarwal, T. Sneideris, F. Svara, K. Jermakovs, H. Coyle, S. Qamar, E. Kava, R. Scrutton, N. Pleschka, P. Peres, *et al.*, *bioRxiv*, 2025 (2025).
 - [14] H. R. Kilgore, I. Chinn, P. G. Mikhael, I. Mitnikov, C. Van Dongen, G. Zylberberg, L. Afeyan, S. F. Banani, S. Wilson-Hawken, T. I. Lee, and R. Barzilay, *Science* **387**, 1095 (2025).
 - [15] K. Kappel, D. Strebing, K. K. Edmonds, S. Chaudy-Tam VO, C. M. Vockley, T. Biswas, S. L. Farhi, R. Macrae, F. Zhang, and A. Regev, *Nat. Methods* **22**, 1464 (2025).

- [16] J. Wessén, N. De La Cruz, H. Lyons, H. S. Chan, and B. R. Sabari, *Commun. Chem.* **8**, 304 (2025).
- [17] K. L. Saar, A. S. Morgunov, R. Qi, W. E. Arter, G. Krainer, A. A. Lee, and T. P. J. Knowles, *Proc. Natl. Acad. Sci. U.S.A.* **118**, e2019053118 (2021).
- [18] Z. Chen, C. Hou, L. Wang, C. Yu, T. Chen, B. Shen, Y. Hou, P. Li, and T. Li, *Proc. Natl. Acad. Sci. U.S.A.* **119**, e2115369119 (2022).
- [19] A. Hadarovich, H. R. Singh, S. Ghosh, M. Scheremetjew, N. Rostam, A. A. Hyman, and A. Toth-Petroczy, *Nat. Commun.* **15**, 10668 (2024).
- [20] K. L. Saar, R. M. Scrutton, K. Blozelyte, A. S. Morgunov, L. L. Good, A. A. Lee, S. A. Teichmann, and T. P. Knowles, *Nat. Commun.* **15**, 5418 (2024).
- [21] S. von Bülow, G. Tesei, F. K. Zaidi, T. Mittag, and K. Lindorff-Larsen, *Proc. Natl. Acad. Sci. U.S.A.* **122**, e2417920122 (2025).
- [22] H. Yang, K. You, L. Ma, X. Wang, G. Pei, and T. Li, *Nat. Commun.* (2026).
- [23] K. E. Gilroy and J. N. Barr, *bioRxiv*, 2026 (2026).
- [24] J. Wang, J.-M. Choi, A. S. Holehouse, H. O. Lee, X. Zhang, M. Jahnel, S. Maharana, R. Lemaitre, A. Pozniakovskiy, D. Drechsel, *et al.*, *Cell* **174**, 688 (2018).
- [25] E. W. Martin, A. S. Holehouse, I. Peran, M. Farag, J. J. Inicco, A. Bremer, C. R. Grace, A. Soranno, R. V. Pappu, and T. Mittag, *Science* **367**, 694 (2020).
- [26] J. Sun, J. Qu, C. Zhao, X. Zhang, X. Liu, J. Wang, C. Wei, X. Liu, M. Wang, P. Zeng, *et al.*, *Nat. Commun.* **15**, 2662 (2024).
- [27] Y. Zhang, J. Zheng, and B. Zhang, *Elife* **14**, RP105309 (2025).
- [28] K. M. Ruff, M. R. King, A. W. Ying, V. Liu, A. Pant, W. E. Lieberman, M. K. Shinn, X. Su, C. Kadoch, and R. V. Pappu, *Cell* **189**, 323 (2026).
- [29] K. L. Saar, D. Qian, L. L. Good, A. S. Morgunov, R. Collepardo-Guevara, R. B. Best, and T. P. Knowles, *Chem. Rev.* **123**, 8988 (2023).
- [30] A. Rizuan, S. Rekh, Y. C. Kim, S. Najafi, J.-E. Shea, and J. Mittal, *Ann. Rev. Phys. Chem.* **77** (2026).
- [31] G. Tesei, A. I. Trolle, N. Jonsson, J. Betz, F. E. Knudsen, F. Pesce, K. E. Johansson, and K. Lindorff-Larsen, *Nature* **626**, 897 (2024).
- [32] B. Novak, J. M. Lotthammer, R. J. Emenecker, and A. S. Holehouse, *Nature*, 1 (2026).
- [33] G. L. Dignon, W. Zheng, Y. C. Kim, R. B. Best, and J. Mittal, *PLoS Comp. Biol.* **14**, e1005941 (2018).
- [34] G. Tesei, T. K. Schulze, R. Crehuet, and K. Lindorff-Larsen, *Proc. Natl. Acad. Sci. U.S.A.* **118**, e2111696118 (2021).
- [35] J. A. Joseph, A. Reinhardt, A. Aguirre, P. Y. Chew, K. O. Russell, J. R. Espinosa, A. Garaizar, and R. Collepardo-Guevara, *Nat. Comput. Sci.* **1**, 732 (2021).
- [36] I. Yasuda, E. Yamamoto, K. Yasuoka, and K. Lindorff-Larsen, *bioRxiv*, 2025 (2025).
- [37] Y.-H. Lin, J. P. Brady, H. S. Chan, and K. Ghosh, *J. Chem. Phys.* **152**, 045102 (2020).
- [38] K. Ghosh, J. Huihui, M. Phillips, and A. Haider, *Ann. Rev. Biophys.* **51**, 355 (2022).
- [39] A. Statt, H. Casademunt, C. P. Brangwynne, and A. Z. Panagiotopoulos, *J. Chem. Phys.* **152**, 075101 (2020).
- [40] S.-F. Li and M. Muthukumar, *Macromolecules* **55**, 5535 (2022).
- [41] M. Phillips, M. Muthukumar, and K. Ghosh, *PNAS Nexus* **3**, pgae367 (2024).
- [42] J. Wessén, S. Das, T. Pal, and H. S. Chan, *J. Phys. Chem. B* **126**, 9222 (2022).
- [43] K. Adachi and K. Kawaguchi, *Phys. Rev. X* **14**, 031011 (2024).
- [44] G. M. Ginell, R. J. Emenecker, J. M. Lotthammer, A. T. Keeley, S. P. Plassmeyer, N. Razo, E. T. Usher, J. F. Pelham, and A. S. Holehouse, *Science* **388**, eadq8381 (2025).
- [45] R. H. Colby and M. Rubinstein, *Polymer physics* (Oxford University Press, 2003).
- [46] F. Chen and W. M. Jacobs, *J. Chem. Theory Comput.* **20**, 6881 (2024).
- [47] W. M. Jacobs and D. Frenkel, *Biophys. J.* **112**, 683 (2017).
- [48] W. M. Jacobs, *Phys. Rev. Lett.* **126**, 258101 (2021).
- [49] D. Zwicker and L. Laan, *Proc. Natl. Acad. Sci. U.S.A.* **119**, e2201250119 (2022).
- [50] F. Chen and W. M. Jacobs, *J. Chem. Phys.* **158**, 214118 (2023).
- [51] D. Qian, H. Ausserwoger, T. Sneideris, M. Farag, R. V. Pappu, and T. P. J. Knowles, *Proc. Natl. Acad. Sci. U.S.A.* **121**, e2407453121 (2024).
- [52] S. Mao, D. Kuldinow, M. P. Haataja, and A. Košmrlj, *Soft Matter* **15**, 1297 (2019).
- [53] M. C. Cohan, M. K. Shinn, J. M. Lalmansingh, and R. V. Pappu, *J. Mol. Biol.* **434**, 167373 (2022).
- [54] A. H. Mao, S. L. Crick, A. Vitalis, C. L. Chicoine, and R. V. Pappu, *Proc. Natl. Acad. Sci. U.S.A.* **107**, 8183 (2010).
- [55] W. Zheng, G. Dignon, M. Brown, Y. C. Kim, and J. Mittal, *J. Phys. Chem. Lett.* **11**, 3408 (2020).
- [56] T. Firman and K. Ghosh, *J. Chem. Phys.* **148**, 123305 (2018).
- [57] R. K. Das and R. V. Pappu, *Proc. Natl. Acad. Sci. U.S.A.* **110**, 13392 (2013).
- [58] Z. Lin, H. Akin, R. Rao, B. Hie, Z. Zhu, W. Lu, N. Smetanin, *et al.*, *Science* **379**, 1123 (2023).
- [59] T. Pal, J. Wessén, S. Das, and H. S. Chan, *J. Phys. Chem. Lett.* **15**, 8248 (2024).
- [60] G. Pei, X. Wang, D. Geng, Z. Chen, W. Xu, T. Li, and P. Li, *bioRxiv*, 2024 (2024).
- [61] A. Agrawal, Y. N. Fang, S. Rizvi, N. F. Noor Azman, M. V. Tirrell, A. Karim, and A. E. Neitzel, *Macromolecules* **58**, 7776 (2025).
- [62] J. Song and S. Ermon, *arXiv preprint arXiv:1910.06222* (2019).
- [63] U. Rana, K. Xu, A. Narayanan, M. T. Walls, A. Z. Panagiotopoulos, J. L. Avalos, and C. P. Brangwynne, *Nat. Chem.* **16**, 1073 (2024).
- [64] A. P. Thompson, H. M. Aktulga, R. Berger, D. S. Bolintineanu, W. M. Brown, P. S. Crozier, P. J. in 't Veld, A. Kohlmeyer, S. G. Moore, T. D. Nguyen, R. Shan, M. J. Stevens, J. Tranchida, C. Trott, and S. J. Plimpton, *Comp. Phys. Comm.* **271**, 108171 (2022).
- [65] M. Zaheer, S. Kottur, S. Ravanbakhsh, B. Poczós, R. R. Salakhutdinov, and A. J. Smola, in *Adv. Neur. Inf. Proc. Sys.*, Vol. 30 (2017).
- [66] D. Frenkel and B. Smit, *Understanding molecular simulation: From algorithms to applications* (Elsevier, 2001).

Supplementary Information for “A thermodynamic metric quantitatively predicts disordered protein partitioning and multicomponent phase behavior”

CONTENTS

I. Extended methods	1
A. Curation of IDR fragments	1
B. Generation of mutant fragments	2
C. Machine-learning framework for free energy prediction	4
D. Proof of completeness	4
E. Encoder architecture and implementation	6
F. General decoder architecture and implementation	6
G. Pairwise decoder architecture and implementation	6
H. Latent space transformation and alignment	8
I. Proof of uniqueness	10
J. Coarse-grained force field	11
K. Equation-of-state simulations	11
L. Model training, validation, and EOS testing procedures	12
M. Calculation of free-energy differences from simulation	12
N. Comparison with hand-crafted mean-field models	13
O. Prediction of multicomponent phase diagrams	14
P. Simulation of phase coexistence and comparison with predicted phase behavior	15
Q. Prediction of multicomponent condensation	16
R. Analysis of point mutation distances	17
S. Theoretical sequence descriptors	17
T. Explained variance and canonical correlation analysis of theoretical descriptors	19
U. Mutual information analysis	20
V. Counterfactual analyses using mutant fragments	21
II. Data sets and computational resources used	24
References	25

I. EXTENDED METHODS

A. Curation of IDR fragments

IDR fragments were collected from a dataset of 28,058 full-length IDRs spanning 15,424 distinct proteins in the human proteome, which was previously reported by Tesei et al.¹. For each full-length IDR, fragment extraction was initiated with a 20-residue segment (20-mer) centered within the sequence. Additional 20-mers were subsequently generated by translating the 20-residue window in both the N-terminal and C-terminal directions using a step size of 10 residues, continuing until insufficient residues remained to construct a new 20-mer. This procedure avoids extracting neighboring 20-mers with greater than 50% identity in any single full-length IDR sequence by construction. In this way, we generated a total of

335,439 20-mers, which were then randomly divided into a training set of 235,439 20-mers for model training and validation and a test set of 100,000 20-mers.

B. Generation of mutant fragments

We generated mutant sequences for each wild-type (WT) sequence in the test set. Whereas the WT IDR fragments are empirical samples from an underlying sequence distribution ρ_{seq} , uniform sampling of mutations does not in general produce mutant (MUT) sequences from the same distribution. We therefore estimated $\ln \rho_{\text{seq}}(s_{\text{MUT}})/\rho_{\text{seq}}(s_{\text{WT}})$ by evaluating the difference between the pseudo log-likelihoods (PLL) of the MUT and WT sequences in the protein language model ESM2 (esm2.t6.8M.UR50D)². To avoid ESM2 artifacts involving the ends of sequences, we performed PLL calculations with sequences embedded in their native context within the full-length human IDR (or polyglycine for sequences with insufficient native context). We used a fixed context window extending three positions at either end of the sequence for this purpose. We then either sampled multiple-mutation sequences using a Markov chain Monte Carlo (MCMC) scheme in accordance with the ESM2 proxy for ρ_{seq} , or we exhaustively enumerated all point-mutation or unique single-swap mutant sequences and used the ESM2 proxy for ρ_{seq} to weight each sequence in the calculation of sequence-ensemble averages.

1. MCMC sequence generation of multi-swap mutants

We used MCMC to stochastically sample composition-preserving variants of each WT IDR fragment in the test set. This scheme is designed to explore the space of local rearrangements of the WT residues while remaining close to the WT sequence and avoiding sequences that are implausible under the language model.

a. Loss function. Let \mathcal{A} denote the standard 20-amino-acid alphabet, and let

$$s = (s_1, \dots, s_L) \in \mathcal{A}^L \tag{S1}$$

be a protein sequence of fixed length L . For a given sequence s , we compute

$$\text{PLL}(s) = \sum_{l=1}^L \log p_{\theta}(s_l \mid s_{-l}, \text{context}), \tag{S2}$$

where $p_{\theta}(\cdot)$ is the masked-language model and the sum only runs over positions within the sequence. Each term in the PLL calculation is conditioned on the sequence at all positions other than the masked position l , s_{-l} , as well as the fixed context window extending three positions beyond each end of the sequence. In addition, we measure similarity to the WT sequence s_{WT} using the Hamming distance

$$d_{\text{H}}(s, s_{\text{WT}}) = \sum_{l=1}^L \mathbf{1}[s_l \neq (s_{\text{WT}})_l]. \tag{S3}$$

We then define the hinge loss

$$H(s) = \max(0, \text{PLL}(s_{\text{WT}}) - \text{PLL}(s)), \quad (\text{S4})$$

which penalizes sequences whose PLL falls below that of the WT, but does not reward sequences with higher-than-WT PLL. This prevents the chain from drifting toward overly predictable model attractors. The MCMC sampler targets the unnormalized distribution

$$\pi(s) \propto \exp\left(-\frac{H(s) + \lambda d_H(s, s_{\text{WT}})}{T}\right), \quad (\text{S5})$$

where $T > 0$ is a fictitious temperature parameter and $\lambda \geq 0$ controls the strength of the penalty for deviating from the WT.

b. Metropolis–Hastings algorithm. The state space for MCMC sampling consists of all permutations of the WT sequence residues. A proposal is generated by sampling $n_{\text{swap}} \sim \text{Uniform}\{1, \dots, 4\}$ and applying n_{swap} random swap moves, each of which exchanges two positions in the sequence. This proposal preserves amino-acid composition exactly and is symmetric. Given a current state s and a proposal s' , the Metropolis–Hastings acceptance probability is

$$\alpha = \min\left(1, \exp\left(-\frac{[H(s') - H(s)] + \lambda[d_H(s', s_{\text{WT}}) - d_H(s, s_{\text{WT}})]}{T}\right)\right). \quad (\text{S6})$$

In the production run, we initialized each chain at the WT sequence, ran for a burn-in period of 200 MCMC steps, and then advanced the chain in fixed-length blocks of 80 MCMC steps to obtain uncorrelated samples. After each block, the current sequence was recorded if it was distinct from the WT and from previously recorded samples. Sampling was performed using $T = 1$ and $\lambda = 1.75$ and continued until nine unique MUT sequences were generated per WT sequence.

2. Unique single-swap generation

We deterministically enumerated all composition-preserving variants that can be obtained from each WT IDR fragment in the test set via a single swap of two residues. For a WT sequence s_{WT} , unique single-swap mutants are defined as

$$s_{(l,l')} = \text{swap}(s_{\text{WT}}, l, l'), \quad \text{for } l < l' \text{ and } (s_{\text{WT}})_l \neq (s_{\text{WT}})_{l'}. \quad (\text{S7})$$

Each resulting sequence differs from the WT by exactly one swap, preserves amino-acid composition, and is guaranteed to be distinct from the WT. For each mutant, we computed PLL using the same definition as in the MCMC framework.

3. Point mutation generation

We deterministically enumerated all single-residue substitutions (i.e., point mutations) of each WT IDR fragment in the test set. Unlike the swap-based methods, this procedure does not preserve amino-acid composition, but instead provides a complete local landscape

of single-site effects. For each position $l \in \{1, \dots, L\}$ and each amino acid $a \in \mathcal{A} \setminus \{(s_{\text{WT}})_l\}$, a mutant $s_{(l \rightarrow a)}$ is generated by substituting the residue at position l with a . This procedure yields exactly $19L$ mutants per WT IDR fragment. For each mutant, we computed PLL using the same definition as in the MCMC framework.

C. Machine-learning framework for free energy prediction

In our framework, an encoder maps each sequence to a feature vector, the feature vectors of different sequences in a mixture combine linearly, and a decoder predicts the excess free-energy density of the mixture from the mixture representation. In this section and in what follows, we use the $\tilde{\cdot}$ notation to indicate that the learned vectors and functions live in an arbitrary coordinate system, which will be transformed later to construct the thermodynamic metric space.

We map each IDR sequence into a learned latent space $\tilde{z} \in \mathbb{R}^d$. Because Mpipi simulations do not distinguish between the N- and C-termini of polypeptide chains, the latent representation is defined as the average of the raw encoder outputs for the original sequence s and its reverse s^{rev} ,

$$\tilde{z} = \tilde{\phi}(s) = (\tilde{\phi}_{\text{raw}}(s) + \tilde{\phi}_{\text{raw}}(s^{\text{rev}}))/2. \quad (\text{S8})$$

For a mixture of IDRs, the mixture’s latent representation is given by the concentration-weighted linear combination of its components,

$$\tilde{x} = \sum_{i=1}^n c_i \tilde{z}_i, \quad (\text{S9})$$

where c_i is the number concentration of component i and n is the number of components in the mixture.

A decoder then maps the mixture representation \tilde{x} to the excess free-energy density of the mixture, from which we obtain thermodynamic quantities. We define the excess free-energy density of the mixture as

$$\hat{f}^{\text{ex}} = \tilde{\Psi}(\tilde{x}) = \tilde{x} \tilde{G}(\tilde{x}) \tilde{x}^{\text{T}}, \quad (\text{S10})$$

where $\tilde{G}(\tilde{x}) \in \mathbb{R}^{d \times d}$ is a symmetric matrix-valued analytic function. All learnable parameters of the decoder enter through $\tilde{G}(\tilde{x})$. This construction is invariant to permutation of sequences in a mixture and obeys the ideal gas law in the low-concentration limit. The excess pressure \hat{P}^{ex} and excess chemical potential $\hat{\mu}^{\text{ex}}$ can be derived by taking derivatives of \hat{f}^{ex} ,

$$\hat{P}^{\text{ex}} = \tilde{x} \cdot \nabla_{\tilde{x}} \tilde{\Psi}(\tilde{x}) - \tilde{\Psi}(\tilde{x}), \quad (\text{S11})$$

$$\hat{\mu}_i^{\text{ex}} = \tilde{z}_i \cdot \nabla_{\tilde{x}} \tilde{\Psi}(\tilde{x}). \quad (\text{S12})$$

D. Proof of completeness

In this section, we show that a linear latent space for molecular sequences together with the prescribed decoder form can represent any analytic and extensive excess free-energy density function, provided that the latent-space dimension d is sufficiently large.

Because the excess free energy F^{ex} of a mixture is invariant under permutations of molecules, it is a set function of the individual molecules. By Theorem 2 of Zaheer et al.³, any permutation-invariant function admits a decomposition of the form

$$F^{\text{ex}} = \tilde{\psi}_V \left(\sum_{j=1}^M \tilde{\phi}_V(s_j) \right), \quad (\text{S13})$$

where s_j denotes the sequence of the j -th molecule, $\tilde{z}_j = \tilde{\phi}(s_j)$ is its latent representation, M is the total number of molecules in the mixture, and $\tilde{\phi}_V$ and $\tilde{\psi}_V$ are suitable nonlinear transformations for a given system volume V .

Grouping identical molecular species yields

$$F^{\text{ex}} = \tilde{\psi}_V \left(\sum_{i=1}^n N_i \tilde{\phi}_V(s_i) \right) = \tilde{\psi}_V \left(\sum_{i=1}^n c_i V \tilde{\phi}_V(s_i) \right), \quad (\text{S14})$$

where n is the number of components in the mixture, N_i is the number of molecules of component i , and $c_i = N_i/V$ is the number concentration.

To enable extrapolation to the thermodynamic limit, we require extensivity of the excess free energy,

$$F^{\text{ex}}(V, \{N_i\}) = V f^{\text{ex}}(\{c_i\}). \quad (\text{S15})$$

Therefore,

$$f^{\text{ex}} = \frac{1}{V} F^{\text{ex}} = \frac{1}{V} \tilde{\psi}_V \left(\sum_{i=1}^n c_i V \tilde{\phi}_V(s_i) \right). \quad (\text{S16})$$

Defining

$$\tilde{\Psi}_V(x) = \frac{1}{V} \tilde{\psi}_V(Vx), \quad (\text{S17})$$

we obtain

$$f^{\text{ex}} = \tilde{\Psi}_V \left(\sum_{i=1}^n c_i \tilde{\phi}_V(s_i) \right). \quad (\text{S18})$$

Since f^{ex} is intensive, this expression must be invariant with respect to V . For any fixed reference volume V_0 ,

$$\tilde{\Psi}_V \left(\sum_{i=1}^n c_i \tilde{\phi}_V(s_i) \right) = \tilde{\Psi}_{V_0} \left(\sum_{i=1}^n c_i \tilde{\phi}_{V_0}(s_i) \right) \quad \text{for all } V. \quad (\text{S19})$$

We therefore define

$$f^{\text{ex}} = \tilde{\Psi} \left(\sum_{i=1}^n c_i \tilde{\phi}(s_i) \right) := \tilde{\Psi}_{V_0} \left(\sum_{i=1}^n c_i \tilde{\phi}_{V_0}(s_i) \right). \quad (\text{S20})$$

Consistency with the ideal-gas limit requires that f^{ex} vanishes faster than linearly as $c_i \rightarrow 0$ for all components i . Because f^{ex} is analytic, this implies that, without loss of generality,

$$\tilde{\Psi}(\tilde{x}) = \tilde{x} \tilde{G}(\tilde{x}) \tilde{x}^{\text{T}}, \quad (\text{S21})$$

where $\tilde{G}(\tilde{x})$ is an analytic, input-dependent matrix that captures higher-order interactions while preserving the correct low-density limit.

We then investigate the number of dimensions required for the latent space $\tilde{z}_i = \tilde{\phi}(s_i)$. While the decomposition in Eq. (S13) is theoretically possible with a one-dimensional latent space, prior work has shown that this often necessitates highly discontinuous mappings. Instead, representing a generic permutation-invariant function with learnable $\tilde{\phi}$ and $\tilde{\psi}$ requires a latent dimension d that scales with the largest set size⁴. In the above formulation of molecular mixtures, the set size is the number of molecules, which is determined by the system size V . In the thermodynamic limit, the number of molecules diverges. In practice, however, high accuracy can often be achieved with latent dimensions much smaller than the maximum set size. We further expect that the latent dimension required for accurate predictions remains bounded in the thermodynamic limit, consistent with the usual statistical-mechanics arguments underlying extensivity.

We therefore conclude that, given a sufficiently large latent-space dimension d , this framework can represent any excess free-energy density corresponding to an analytic and extensive free energy that is permutation invariant with respect to the molecules in the mixture. In practice, the latent dimension required to achieve a desired prediction accuracy must be determined empirically, as demonstrated in this work.

E. Encoder architecture and implementation

Each IDR sequence is tokenized into discrete residue tokens and processed by a three-layer Transformer raw encoder with two attention heads, a model dimension of 16, and a feed-forward dimension of 48. The Transformer outputs are mapped to the latent space via a learnable linear projection. The encoder output is the average of the raw outputs for the original sequence and its reverse, as in Eq. (S8).

F. General decoder architecture and implementation

To implement a general decoder, we parameterize the symmetric matrix-valued function $\tilde{G}(\tilde{x})$ using an artificial neural network. The $d(d+1)/2$ independent entries of the upper triangular part of $\tilde{G}(\tilde{x})$ are parameterized by a multilayer perceptron (MLP) with 2 hidden layers of 128 and 64 neurons, respectively. To ensure $\tilde{G}(\tilde{x})$ is analytic, the SiLU activation function is used. The full symmetric matrix is constructed by mirroring the upper triangular entries across the diagonal.

Given $\tilde{G}(\tilde{x})$, the excess free-energy density is computed as $\tilde{\Psi}(\tilde{x}) = \tilde{x} \tilde{G}(\tilde{x}) \tilde{x}^\top$, and \hat{P}^{ex} and $\hat{\mu}^{\text{ex}}$ are calculated by automatic differentiation. We refer to the model implemented using this general decoder as the ‘‘MLP model’’ in the main text.

G. Pairwise decoder architecture and implementation

The pairwise decoder is a specific, constrained form of the general decoder designed to recover a pairwise interaction structure. In this formulation, all sequence-dependent contributions to the free energy enter through pairwise interactions between latent sequence

representations, analogous to classical mean-field models such as Flory–Huggins (FH). However, in contrast to the standard FH model, pairwise coefficients in our decoder describe interactions between polymers as opposed to monomers and can thus in principle account for sequence-dependent patterning effects. Higher-order concentration effects are retained only through powers of the total concentration, capturing sequence-independent excluded-volume contributions.

The excess free-energy density within this pairwise approximation is

$$\hat{f}^{\text{ex}} = \frac{1}{2} \tilde{x} \tilde{G}^{\text{PW}} \tilde{x}^{\text{T}} + \sum_{p=3}^{20} \frac{\tilde{a}_p}{p-1} (\tilde{x}^{(d)})^p. \quad (\text{S22})$$

The symmetric matrix $\tilde{G}^{\text{PW}} \in \mathbb{R}^{d \times d}$ is learned and encodes interaction rules between latent dimensions. In this decoder, \tilde{G}^{PW} is taken to be constant, independent of \tilde{x} . The final latent dimension d represents the effective molecular size and is fixed so that $\tilde{z}_i^{(d)} = 1$ for all i , since all IDR fragments in the sequence ensemble have the same length. As a result, the second term in Eq. (S22), which captures higher-order excluded volume effects, depends only on the total concentration. Specifically, $\tilde{x}^{(d)} = \sum_{i=1}^n c_i = c_{\text{tot}}$, with learned coefficients $\tilde{a}_p > 0$. These choices ensure that all sequence-dependent contributions to \hat{f}^{ex} enter through the quadratic form $\tilde{x} \tilde{G}^{\text{PW}} \tilde{x}^{\text{T}}$.

For a d -dimensional pairwise model, we can write the interaction parameter between components i and j in the recognizable pairwise form

$$\varepsilon_{ij} = \tilde{z}_i \tilde{G}^{\text{PW}} \tilde{z}_j^{\text{T}}, \quad (\text{S23})$$

so that

$$\frac{1}{2} \tilde{x} \tilde{G}^{\text{PW}} \tilde{x}^{\text{T}} = \frac{1}{2} \sum_{i=1}^n \sum_{j=1}^n \varepsilon_{ij} c_i c_j. \quad (\text{S24})$$

From Eq. (S22), the excess pressure is obtained as

$$\begin{aligned} \hat{P}^{\text{ex}} &= \tilde{x} \cdot \nabla_{\tilde{x}} \hat{f}^{\text{ex}} - \hat{f}^{\text{ex}} \\ &= \frac{1}{2} \sum_{i=1}^n \sum_{j=1}^n \varepsilon_{ij} c_i c_j + \sum_{p=3}^{20} \tilde{a}_p (\tilde{x}^{(d)})^p. \end{aligned} \quad (\text{S25})$$

Including the ideal contribution $P^{\text{id}} = c_{\text{tot}} kT$, the total pressure takes the form

$$\hat{P} = c_{\text{tot}} kT + \frac{1}{2} \sum_{i,j=1}^n \varepsilon_{ij} c_i c_j + \sum_{p=3}^{20} \tilde{a}_p (\tilde{x}^{(d)})^p, \quad (\text{S26})$$

which matches the structure of FH-type models: an ideal term, a quadratic pairwise interaction term, and additional higher-order concentration-dependent corrections.

Accordingly, the excess chemical potential of component i is obtained from Eq. (S22) as

$$\begin{aligned}\hat{\mu}_i^{\text{ex}} &= \frac{\partial \hat{f}^{\text{ex}}}{\partial c_i} \\ &= \sum_{j=1}^n \varepsilon_{ij} c_j + \sum_{p=3}^{20} \frac{p}{p-1} \tilde{a}_p (\tilde{x}^{(d)})^{p-1}.\end{aligned}\tag{S27}$$

H. Latent space transformation and alignment

This section describes a physically motivated linear transformation of the latent space of each trained model, defined by the $L_2(\rho_{\text{mix}})$ norm of the excess chemical potential $\hat{\mu}^{\text{ex}}$. This norm endows the latent space $\tilde{z} \in \mathbb{R}^d$ of each trained model with a consistent metric, producing a shared metric space $z \in \mathbb{R}^d$ in which the positions of sequences correspond directly to the physical μ^{ex} geometry. We first introduce a principled strategy for sampling mixtures. We then define a metric space such that Euclidean distances correspond directly to the norm of differences between μ^{ex} functions. Lastly, we canonicalize the metric-normalized coordinates using orthogonal transformations around the origin, resulting in a single aligned metric space across all trained models.

1. Mixture prior

We consider mixtures of n different sequences sampled from the IDR fragment ensemble with concentrations $c_i \geq 0$ and total concentration $c_{\text{tot}} = \sum_{i=1}^n c_i$. The sequences are chosen uniformly and independently from this set. We parameterize mixtures by the total concentration c_{tot} and mole fraction c_i/c_{tot} . We further assume that the prior distribution over mixtures, ρ_{mix} , factorizes as

$$\rho_{\text{mix}}(c) = p(c_{\text{tot}}) p(c/c_{\text{tot}}),\tag{S28}$$

with $c_{\text{tot}} \sim \text{Uniform}(0, c_{\text{tot,max}}]$ and $(c/c_{\text{tot}}) \sim \text{Dirichlet}(\alpha, \dots, \alpha)$ over all n sequences. We set $c_{\text{tot,max}} = 0.25 \text{ chains/nm}^3$ and choose the symmetric Dirichlet parameter as $\alpha = \tilde{\alpha}/n$, where $\tilde{\alpha} = O(1)$ is a fixed total concentration. In the large- n limit this yields sparse mole fractions with an $O(1)$ effective cardinality. In this work, we chose the value of $\tilde{\alpha}$ empirically to achieve a desired effective cardinality threshold of $|\{i : c_i/c_{\text{tot}} > \varepsilon\}| \sim 2.5$ with $\varepsilon \approx 10^{-2}$. This prior distribution places support over all mixtures that can be composed from the n sequences in the IDR fragment ensemble, while biasing toward relatively sparse mole fractions in which only a small subset of sequences is strongly enriched.

To sample mole fractions, we use a stick-breaking (GEM) construction⁵ with parameter $\tilde{\alpha}$:

$$v_i \sim \text{Beta}(1, \tilde{\alpha}), \quad w_i = v_i \prod_{j<i} (1 - v_j),\tag{S29}$$

where the weights w_i represent the mole fractions of the selected sequences. The construction is truncated once the remaining mass is below a tolerance of 10^{-6} . The weights $\{w_i\}$ are renormalized and assigned to randomly chosen distinct sequence indices. This procedure samples exactly from the symmetric Dirichlet distribution in the $n \rightarrow \infty$ limit.

2. Metric definition

For each trained model $k = 1, \dots, K$, we define

$$M^{(k)} = \int d\tilde{x} \rho_{\text{mix}}(\tilde{x}) \nabla \tilde{\Psi}^{(k)}(\tilde{x}) \nabla \tilde{\Psi}^{(k)}(\tilde{x})^\top, \quad (\text{S30})$$

which is symmetric positive semidefinite and induces the $L_2(\rho_{\text{mix}})$ norm

$$\|\hat{\mu}_i^{\text{ex},(k)}\|_{L_2(\rho_{\text{mix}})}^2 = \tilde{z}_i^{(k)} M^{(k)} (\tilde{z}_i^{(k)})^\top. \quad (\text{S31})$$

We estimate $M^{(k)}$ by Monte Carlo sampling from the prior, ρ_{mix} . For each draw, we sample c/c_{tot} by stick breaking, sample c_{tot} , form

$$\tilde{x}^{(k)} = c_{\text{tot}} \sum_i (c_i/c_{\text{tot}}) \tilde{z}_i^{(k)}, \quad (\text{S32})$$

evaluate $g^{(k)} = \nabla \Psi^{(k)}(x^{(k)})$, and accumulate $g^{(k)}(g^{(k)})^\top$. Averaging over samples yields the Monte Carlo estimate $\widehat{M}^{(k)}$. Finally, using $A^{\text{trans},(k)} = (\widehat{M}^{(k)})^{1/2}$ to denote the principal positive semidefinite square root, we define transformed latent coordinates

$$z_i^{\text{trans},(k)} = \tilde{z}_i^{(k)} (A^{\text{trans},(k)})^\top, \quad (\text{S33})$$

so that

$$\|z_i^{\text{trans},(k)}\|_2^2 = \tilde{z}_i^{(k)} \widehat{M}^{(k)} (\tilde{z}_i^{(k)})^\top. \quad (\text{S34})$$

3. Canonicalization and alignment

For each model, we perform uncentered principal component analysis (PCA) on $z^{\text{trans},(k)}$. Specifically, we diagonalize $(1/n)(Z^{\text{trans},(k)})^\top Z^{\text{trans},(k)}$, where the rows of $Z^{\text{trans},(k)}$ are $z_i^{\text{trans},(k)}$ for all sequences i in the IDR fragment ensemble, rotate into the PCA basis, and fix the sign of each axis by requiring the mean coordinate to be nonnegative. This removes arbitrary rotations and reflections within each model.

Starting from the PCA-canonicalized coordinates, we note that for a perfect model the resulting metric space is already unique up to an orthogonal transformation (see Sec. II). Thus, no further alignment should be required in principle. In practice, however, small discrepancies arise because the trained models are imperfect. To reduce residual misalignment across the K models, we apply generalized orthogonal Procrustes to optimize their alignment in a common frame. We find that this step results in only minor rotational adjustments, since the per-model PCA-canonicalized coordinates are already extremely similar.

We then define a global canonical basis by applying uncentered PCA to the mean (aligned) model, with the same sign convention, and rotate all models into this basis. The resulting aligned coordinates satisfy

$$z_i^{(k)} = \tilde{z}_i^{(k)} (A^{(k)})^\top, \quad (\text{S35})$$

where $A^{(k)} = O^{(k)} A^{\text{trans},(k)}$ folds together the metric square root and all subsequent orthogonal transformations. For each model, the excess free energy in the aligned coordinate system

becomes

$$\hat{f}^{\text{ex},(k)} = \Psi^{(k)}(x^{(k)}), \quad (\text{S36})$$

where

$$x^{(k)} = \sum_i c_i z_i^{(k)} = \tilde{x}^{(k)}(A^{(k)})^\top, \quad (\text{S37})$$

$$\Psi^{(k)}(x^{(k)}) = x^{(k)}(A^{(k)})^{-\top} \tilde{G}^{(k)}(x^{(k)}(A^{(k)})^{-\top}) (A^{(k)})^{-1} (x^{(k)})^\top. \quad (\text{S38})$$

The encoder in the transformed coordinate system becomes

$$\phi^{(k)}(s_i) = z_i^{(k)} = \tilde{\phi}^{(k)}(s_i)(A^{(k)})^\top. \quad (\text{S39})$$

We expect $\phi_i^{(k)}$ and $\Psi^{(k)}$ to be unique for a perfect model (see Sec. II).

We refer to the mean coordinates in this aligned *thermodynamic metric space* obtained from the trained general-decoder MLP models as

$$z_i = \frac{1}{K} \sum_{k=1}^K z_i^{(k)} \quad (\text{S40})$$

in the main text, where we average over the $K = 5$ models from 5-fold cross validation, and we report the uncertainty of each point in this metric space as

$$\text{RMSD}_i = \sqrt{\frac{1}{K} \sum_{k=1}^K (z_i^{(k)} - z_i)^2}. \quad (\text{S41})$$

I. Proof of uniqueness

For any pair of points i, j in the z -space of model k , we have

$$\begin{aligned} \|z_i^{(k)} - z_j^{(k)}\|_2 &= \sqrt{(\tilde{z}_i^{(k)} - \tilde{z}_j^{(k)})(A^{\text{trans},(k)})^\top (O^{(k)})^\top O^{(k)} A^{\text{trans},(k)} (\tilde{z}_i^{(k)} - \tilde{z}_j^{(k)})^\top} \\ &= \sqrt{(\tilde{z}_i^{(k)} - \tilde{z}_j^{(k)}) \widehat{M}^{(k)} (\tilde{z}_i^{(k)} - \tilde{z}_j^{(k)})^\top} \\ &= \|\hat{\mu}_i^{\text{ex},(k)} - \hat{\mu}_j^{\text{ex},(k)}\|_{L_2(\rho_{\text{mix}})}. \end{aligned} \quad (\text{S42})$$

When the model accurately predicts excess chemical potentials, the right-hand side of Eq. (S42) depends only on the physical quantities and is therefore invariant across different models $k = 1, \dots, K$. Consequently, pairwise Euclidean distances between points in the corresponding z -spaces are identical for all accurate models.

In addition, $z_i^{(k)} = \vec{0}$ indicates $\|\mu_i^{\text{ex},(k)}\|_{L_2(\rho_{\text{mix}})} = 0$, which is true if and only if $\mu_i^{\text{ex},(k)} = 0$ for all mixtures. We therefore identify the origin in z -space with an ideal polymer.

Taken together, these results imply that the embeddings $z^{(k)}$ produced by different accurate models preserve all pairwise distances and share a common origin. Any two such embeddings are related by a distance-preserving transformation that fixes the origin. These transformations form the orthogonal group $O(d)$, consisting of rotations and reflections.

Hence, the thermodynamic metric representation is unique up to an orthogonal trans-

formation. The quantity denoted as z in the main text should be treated as one specific aligned choice, based on uncentered PCA, from this equivalence class.

J. Coarse-grained force field

All equation-of-state, free-energy, and phase-coexistence simulations in this work were conducted using the Mpipi force field⁶ implemented in LAMMPS⁷. Mpipi is a state-of-the-art residue-level coarse-grained model for predicting biomolecular phase behavior. In the Mpipi model, each amino acid is represented by a single bead, with specified mass, diameter (σ), charge (q), and an energy scale (ε) for short-range interactions⁶. The potential energy is specified as

$$E_{\text{Mpipi}} = E_{\text{bond}} + E_{\text{elec}} + E_{\text{pair}}. \quad (\text{S43})$$

The bond energy is given by a harmonic bond potential

$$E_{\text{bond}} = \sum_{\text{bonds } i} \frac{1}{2} k (r_i - r_{i,\text{ref}})^2, \quad (\text{S44})$$

where k is set to $8.03 \text{ J mol}^{-1} \text{ pm}^{-2}$, r_i is the bond length, and the reference bond length $r_{i,\text{ref}}$ is 381 pm. The electrostatic interactions are modeled using a Coulomb potential with Debye–Hückel screening

$$E_{\text{elec}} = \sum_{i,j} \frac{q_i q_j}{4\pi\varepsilon_r\varepsilon_0 r_{ij}} \exp(-\kappa r_{ij}), \quad (\text{S45})$$

where $\varepsilon_r = 80$ is the relative dielectric constant of water, ε_0 is the vacuum permittivity, and $\kappa^{-1} = 795 \text{ pm}$ is the Debye screening length corresponding to a monovalent salt concentration of 0.15 mol L^{-1} . The cutoff distance of E_{elec} is set to 3.5 nm.

Nonbonded interactions between amino-acid beads are described by the Wang–Frenkel (WF) potential, which for a pair of beads of types a and b separated by a distance r , is given by

$$\phi_{ab}(r) = \varepsilon_{ab} \left[\left(\frac{\sigma_{ab}}{r} \right)^{2\mu_{ab}} - 1 \right] \left[\left(\frac{R_{ab}}{r} \right)^{2\mu_{ab}} - 1 \right]^{2\nu_{ab}}, \quad (\text{S46})$$

with σ_{ab} , ε_{ab} , and μ_{ab} uniquely defined for each pair of interacting bead types. The parameters ν_{ab} and R_{ab} are set to 1 and $3\sigma_{ab}$, respectively. The total pairwise nonbonded potential energy E_{pair} is computed by summing ϕ_{ab} for all pairs of beads within the corresponding cutoff distances R_{ab} .

K. Equation-of-state simulations

Equation-of-state (EOS) simulations were performed for n -component IDR systems with $n \in \{1, 2, 3, 4\}$. In each simulation, 100 IDR molecules were initialized uniformly in a cubic simulation box at the prescribed mole fractions and total concentration. After energy minimization, the system was simulated for 10 ns with a timestep of 10 fs using Velocity Verlet integration. Pressure was recorded every 1000 timesteps and averaged after a typical equilibration time of 2 ns to generate the EOS data.

All simulations were carried out at 300 K using a Langevin thermostat with a damping

parameter of 1 ps under periodic boundary conditions. The temperature, timestep, and thermostat scheme were chosen to be consistent with prior IDR simulations reported by Joseph et al.⁶.

L. Model training, validation, and EOS testing procedures

To generate the training and validation datasets, we performed simulations for 20,000 unary and 120,000 binary IDR systems (see Sec. II). IDR sequences were randomly drawn from the curated library of 20-mer fragments. For the 20,000 unary systems and 100,000 of the binary systems, the total concentration was randomly sampled from a piecewise-uniform distribution with 20% probability in the range 1×10^{-5} to 1×10^{-3} chains/nm³, 20% in 1×10^{-3} to 0.01 chains/nm³ and 60% in 0.01 to 0.25 chains/nm³. Total concentrations in the other 20,000 binary systems were sampled exclusively from the range 0.01 to 0.25 chains/nm³. For binary mixtures, this total concentration was randomly partitioned between the two sequence types, resulting in uniformly sampled mole fractions.

Models were trained using 5-fold cross-validation. The simulated dataset was randomly partitioned into five folds, with four folds used for training and the remaining fold used for validation. This procedure yielded five models, each validated on a different fold, for each latent-space dimension d . For each split, we trained five replicate models with different random initializations (random seeds) and retained the replicate with the lowest validation loss. Models were trained in PyTorch⁸ and optimized using the Adam optimizer⁹. The transformer encoder used dropout = 0.1. We set the batch size to 2048/4096 and tuned the learning rate using a grid search over $\{0.001, 0.005, 0.01\}/\{0.0001, 0.001, 0.01, 0.1\}$ for the MLP/PW models. For the PW model, two separate optimizers were used for updating the parameters of \tilde{G}^{PW} and the \tilde{a}_p , respectively (see Sec. I G). We used $\text{MSE}(P/c_{\text{tot}})$ as the training loss to emphasize accuracy at low total concentration, which is important for reliable free-energy prediction; this choice also results in relatively uniform simulation uncertainties across total concentrations (Fig. S1a–c). Training used early stopping based on validation loss, and the checkpoint with the lowest validation loss was retained.

For testing, we constructed two classes of datasets in which test-set sequences were drawn either uniformly from the sequence pool or uniformly from the metric space. For each class, we generated test sets for single-component, two-component, three-component, and four-component mixtures. Test-set total concentrations were sampled as in the 20,000 unary and 100,000 binary systems in the training set. Random mole fractions were then sampled by randomly partitioning the total concentration among the n sequence types.

M. Calculation of free-energy differences from simulation

Free-energy test data for selected n -component IDR systems, with $n \in \{1, 2, 3, 4\}$, were obtained by integrating P^{ex} simulation data. For each pair of sequences considered, two mole fractions were randomly selected, except for single-component systems, in which case the mole fraction is always one. EOS simulations were performed for each mole fraction at 80 total concentrations, logarithmically spaced in the range from 1×10^{-5} chain nm⁻³ to 0.25 chain nm⁻³.

The ideal contribution ($c_{\text{tot}}kT$) was subtracted from the simulated EOS data to generate the $P^{\text{ex}}(c_{\text{tot}})$ simulation data for each mole fraction, which was subsequently fitted with

a 100th-order polynomial in c_{tot} starting from the quadratic term. The fitted $P^{\text{ex}}(c_{\text{tot}})$ polynomial was then integrated to obtain the excess free-energy density f^{ex} . The total free-energy density is thus

$$\begin{aligned}
 f &= f^{\text{id}} + f^{\text{ex}} \\
 &= \underbrace{\sum_{i=1}^n c_i (\ln(c_i) - 1)}_{f^{\text{id}}} + \underbrace{\int_0^{c_{\text{tot}}} \frac{P^{\text{ex}}}{r^2} dr}_{f^{\text{ex}}}.
 \end{aligned}
 \tag{S47}$$

For each pair of sequences considered, we applied this procedure to obtain the free-energy density function $f(c_{\text{tot}})$ along each selected ray of constant mole fraction. We then randomly selected one total concentration uniformly from the concentration range along each ray and used the corresponding free-energy densities f_1 and f_2 to define the free-energy density difference $\Delta f = |f_1 - f_2|$. These simulated Δf data formed the test dataset, which was used to evaluate the $\text{RMSE}(\Delta f)$ of the model-predicted free-energy differences, $\widehat{\Delta f}$. For single-component systems, only one free-energy density was sampled, and the free-energy difference was computed as $\Delta f = |f_1 - f^{\text{id}}|$.

Model performance was quantified by repeating this sampling and evaluation procedure 100 times. The $\text{RMSE}(\Delta f)$ values and the associated error bars reported in Fig. 1k represent the mean and standard deviation across these realizations. In the scatter plots shown in Fig. 1j, Fig. S2d, and Fig. S3e,f, we used the realization for which the computed MLP model performance is closest to the reported average.

N. Comparison with hand-crafted mean-field models

The multicomponent Flory–Huggins (FH) model¹⁰ is an analytical theory that invokes a pairwise approximation for polymer interactions. In this model, the free-energy density is

$$\frac{f(\{\phi_i\})v}{kT} = \sum_i \frac{\phi_i}{L} \ln(\phi_i) + (1 - \phi_{\text{tot}}) \ln(1 - \phi_{\text{tot}}) + \frac{1}{2} \sum_i \sum_j \epsilon_{ij} \phi_i \phi_j,
 \tag{S48}$$

where v denotes the FH lattice-site volume, ϕ_i is the volume fraction of sequence i , ϕ_{tot} is the total volume fraction of all IDR sequences in the mixture, and ϵ_{ij} is the pairwise interaction parameter for sequences i and j . The polymer length is $L = 20$ for all IDR fragments in the sequence ensemble in this work. We note that the quadratic interaction term in this equation differs from the standard FH model in that the coefficients ϵ_{ij} represent interactions between chains as opposed to monomers, thus allowing for sequence-dependent interaction parameters.

To compare hand-crafted pairwise free-energy densities with simulation data, we introduced two adjustable parameters, v and λ : the aforementioned FH reference volume v that converts concentration c_i to volume fraction ϕ_i with $\phi_i = L_i c_i v$, and a global scaling factor λ for the interaction FH parameter ϵ_{ij} . With these adjustable parameters included, the EOS derived from the FH free-energy density is

$$\frac{P}{kT} = -\frac{1}{v} \ln(1 - L c_{\text{tot}} v) + c_{\text{tot}}(1 - L) + \frac{1}{2} \lambda v L^2 \sum_i \sum_j \epsilon_{ij} c_i c_j.
 \tag{S49}$$

To optimize these adjustable parameters, we minimized $\text{MSE}(P/c_{\text{tot}})$ using a least squares fit over all 140,000 training data points. Then, to predict the free-energy density consistent with the globally optimized EOS, we computed the excess free-energy density by integrating the excess pressure,

$$\frac{f^{\text{ex}}}{kT} = \frac{1}{v}(1 - Lc_{\text{tot}}v) \ln(1 - Lc_{\text{tot}}v) + \frac{1}{2}\lambda vL^2 \sum_i \sum_j \epsilon_{ij}c_i c_j + Lc_{\text{tot}}. \quad (\text{S50})$$

Finally, we added the ideal contribution, $f^{\text{id}}/kT = \sum_i c_i(\ln c_i - 1)$, to obtain the full free-energy density with the optimized adjustable parameters. This globally optimized free-energy density is used to compute the hand-crafted free-energy density difference test loss in Fig. 1j,k and Fig. S3e,f, and to predict binary phase diagrams for hand-crafted models in Fig. 2e and Fig. S4c.

For FINCHES¹¹, we obtained the unscaled ϵ_{ij} parameters from the output of their function `calculate_epsilon_value` using Mpipi force-field parameters. For Adachi et. al.¹², we first calculated the virial coefficient within the dimer pair approximation B_{ij}^{DP} using Eq. (8) of their paper, and then derived ϵ_{ij} from this coefficient by expanding the FH equation of state. In this case, for self-consistency with the virial expansion, we used the adjustable parameter λ to scale B_{ij}^{DP} instead of ϵ_{ij} (Fig. S3).

O. Prediction of multicomponent phase diagrams

The binary phase diagrams shown in Fig. 2 and Fig. 3 were directly generated from the predicted free-energy densities using a multicomponent generalization of the standard common tangent construction¹³. For a given two-component system, the binary composition space was first discretized into a square lattice, where c_1 and c_2 take values from 0 to 0.25 chain nm^{-3} with a spacing of 0.005 chain nm^{-3} . Grid points with $c_{\text{tot}} > 0.25$ chain nm^{-3} were excluded from consideration, as the average distances between residues fall within the typical repulsive core of the nonbonded potential at these high concentrations (see Sec. IJ). The predicted free-energy densities, \hat{f} , of the binary mixtures corresponding to the resultant 1320 grid points were then computed using Eq. (S47), with the integral term replaced by the excess free-energy density predicted by the model, \hat{f}^{ex} .

The convex hull of the discretized free-energy density surface was then constructed using the algorithm developed by Mao et al.¹³. The constructed convex hull consists of triangular facets that envelop the discretized free-energy density surface from below. Each facet comprises three vertices that define a common tangent plane to this surface. Thus, the phases corresponding to the vertices of each facet satisfy the conditions of equal pressure and equal chemical potentials for all components, and are therefore in thermodynamic coexistence.

Each binary phase diagram was obtained by projecting the constructed convex hull back onto the composition space. For each triangular facet, its vertices were first projected to define a triangle in the composition space. If no free-energy grid point with composition lying inside this triangle was located above the corresponding common-tangent plane, no edges were drawn between the vertices, and the vertices were colored blue to denote a single-phase region. Otherwise, edges were drawn between the projected vertices and colored orange to denote phase-separated regions.

In general, when a projected triangle contains only two elongated edges, it corresponds

to a predicted two-phase region. The elongated edges represent tie-lines connecting the two coexisting phases, while the two vertices joined by the short edge correspond to a single phase whose composition is given by the average of the two vertices. A mixture with a parent (i.e., overall) concentration vector lying within such a triangle is predicted to phase separate into the two phases connected by the tie-line, with volume fractions determined by the lever rule.

When a projected triangle has three elongated edges, its three vertices denote the compositions of three coexisting phases (c^I , c^{II} and c^{III}). A mixture with a parent concentration vector c that resides inside the triangle is predicted to phase separate into these three phases with volume fractions η^I , η^{II} and η^{III} , such that $c = \sum_{\alpha} c^{\alpha} \eta^{\alpha}$ and $\sum_{\alpha} \eta^{\alpha} = 1$ ($\eta^{\alpha} \geq 0$). Three-phase coexistence was, however, neither predicted nor observed in the binary systems chosen for phase diagram investigation.

P. Simulation of phase coexistence and comparison with predicted phase behavior

To sample phase diagrams for testing, we partitioned the metric space uniformly into a 21-cell grid. For the training/validation and held-out sequence sets separately, we selected a representative sequence from within a small hypersphere centered in each grid cell. For each of these sequence sets, we constructed all unique sequence pairs, including homotypic systems, yielding 231 unary or binary systems. We then used our trained model to predict the phase diagram for each system in each test set.

To validate the predicted phase behaviors, we randomly sampled sequence pairs and parent concentrations from the 231 representative phase diagrams in each test set for direct simulation. To ensure balanced coverage of homogeneous and phase-separating mixtures, as well as homotypic (unary) and heterotypic (binary) phase separation, we stratified mixtures according to these categories based on the predicted phase diagrams and sampled separately from each stratum. Within predicted two-phase regions, parent concentrations were chosen at the midpoints of the predicted tie lines. To reduce ambiguous or slow-to-converge simulations, we excluded mixtures predicted to lie near phase boundaries. In total, we obtained 59 test mixtures composed of sequences used in training and validation, and 58 test mixtures composed of held-out sequences.

We performed direct-coexistence simulations of binary mixtures in a slab geometry using 1000 chains with $L_z/L_x = L_z/L_y = 6$. To verify equilibration, four simulations of each mixture were initialized from four distinct configurations: with components initially mixed or demixed, and with sequences initially distributed uniformly throughout the box or confined to half of the box. Simulations were continued until the four realizations converged qualitatively. Trajectories were recorded every 10,000 steps (100 ps). Local concentrations were computed by dividing the long axis z into 50 bins. For each test mixture, the realization exhibiting the smallest fluctuations in the concentration profile over the final 1000 recorded frames was selected for downstream analysis.

For the selected realization of each simulated test mixture, we collected local concentrations of the two sequences, $(c_1^{\text{local}}, c_2^{\text{local}})$, over the final 500 snapshots and estimated their joint distribution by binning samples into $0.005 \text{ chain/nm}^3 \times 0.005 \text{ chain/nm}^3$ bins. This distribution is strongly peaked around the average concentrations of the coexisting bulk phases at equilibrium. To compare model predictions with simulations, we converted the predicted equilibrium phases into a discretized probability distribution on the same concentration grid, assigning probability mass to each (c_1, c_2) bin according to the predicted phase

compositions and their corresponding volume fractions. The predicted and simulated local concentration distributions were compared using the 1-Wasserstein (earth-mover) distance, computed with the `emd` method in the POT package¹⁴.

To account for fluctuations and interfacial contributions to the concentration distributions in the simulations, we computed a best-case (positive-control) 1-Wasserstein distance defined as the minimum distance between the simulated distribution and any binned one-phase or two-phase distribution that preserves the parent concentration in the thermodynamic limit. For two-phase distributions, we enforced a minimum Euclidean separation of 0.05 chain/nm³ between the concentrations of the two phases when constructing the positive control. For each test set, we report the 1-Wasserstein distance between each model prediction and the corresponding simulated concentration distribution, normalized by the lower-bound distance of the positive control. We also constructed a negative control for each test set by pairing simulations with random phase-coexistence predictions that preserve the parent concentration as well as the overall balance between one-phase and two-phase coexistence observed in the test simulations.

Q. Prediction of multicomponent condensation

To predict multicomponent condensation directly from the metric space, we consider a scenario in which one or more high-total-concentration condensed phases coexist with a dilute (i.e., low-total-concentration) phase. The presence of a stable dilute phase at thermodynamic equilibrium implies that the coexistence pressure is near zero, since the pressure in the dilute phase must be near zero according to the ideal gas law. We therefore look for solutions of the equation

$$P(c_{\text{tot}}; \bar{z}) = c_{\text{tot}}kT + P^{\text{ex}}(c_{\text{tot}}\bar{z}) \approx 0, \quad (\text{S51})$$

where $c_{\text{tot}} \geq 0$ is the total concentration and $\bar{z} \in \mathbb{R}^d$ denotes a concentration-weighted average point in the metric space. We emphasize that \bar{z} is related to the putative condensed phase, not the parent concentration of a phase-separated mixture. Only solutions satisfying

$$\frac{dP}{dc_{\text{tot}}} > 0 \quad (\text{S52})$$

are retained, as these correspond to phases that are stable at local thermodynamic equilibrium. We ignore the trivial solution at $c_{\text{tot}} = 0$, which corresponds to the dilute phase in this $P \approx 0$ approximation.

By determining whether nontrivial solutions to Eq. (S51) and Eq. (S52) exist at a particular value of \bar{z} , we can immediately conclude whether a condensed phase with mixture representation \bar{z} can coexist with a dilute phase within the $P \approx 0$ approximation. Importantly, this solution does not specify how \bar{z} is constructed: it can represent the feature vector of a single sequence, or it can represent the concentration-weighted average of the feature vectors of many distinct sequences in a mixture, in which case \bar{z} must lie within the convex hull of the feature vectors of those sequences.

We note that the existence of a solution to Eq. (S51) and Eq. (S52) does not necessarily imply that a condensed phase with mixture representation \bar{z} will be stable at global thermodynamic equilibrium in a multicomponent mixture, since there may in general be

competing phases whose free energies must also be considered. Moreover, we note that this approach does not predict how many distinct condensed phases are in coexistence with the dilute phase. Finally, we emphasize that this construction only determines whether a condensed phase can coexist with a dilute phase; it does not indicate whether other types of phase-separated states, specifically those in which none of the coexisting phases are dilute, are possible.

In practice, we solved Eq. (S51) for $c_{\text{tot}} \in (0, c_{\text{tot}}^{\text{max}} = 0.25 \text{ chains/nm}^3]$ by bracketing roots on a uniform grid in c_{tot} and refining candidate solutions using a scalar root-finding algorithm. We retained the solution with the lowest c_{tot} if multiple solutions were found. For visualization purposes, we performed these calculations on a two-dimensional lattice in \bar{z} , which was selected by taking a slice of the full d -dimensional metric space. We then identified both an example single sequence s_i whose feature vector lies within $\sim \text{RMSD}_i$ of a lattice point with a solution to Eq. (S51), and a pair of sequences (s_i, s_j) for which the line segment between their feature vectors passes within $\sim \max(\text{RMSD}_i, \text{RMSD}_j)$ of a lattice point with a solution to Eq. (S51).

R. Analysis of point mutation distances

We used the metric property of our model to compute the average effect size of single substitutions from amino-acid type $a \in \mathcal{A}$ to amino-acid type $b \in \mathcal{A}$. For each WT sequence in the test set, let z_{WT} denote the feature vector of the WT sequence and let z_m denote the feature vector of a single-substitution mutant indexed by $m \in \{1, \dots, 19L\}$ derived from that WT sequence.

Let $\mathcal{M}(a \rightarrow b)$ be the set of all single-substitution mutants derived from a WT sequence whose substitution is $a \rightarrow b$. To compute the average effect size, we first compute the PLL-weighted average displacement in the metric space for each substitution type given a WT sequence,

$$\Delta z(a \rightarrow b) = \frac{\sum_{m \in \mathcal{M}(a \rightarrow b)} w_m |z_m - z_{\text{WT}}|}{\sum_{m \in \mathcal{M}(a \rightarrow b)} w_m}, \quad (\text{S53})$$

with weights $w_m \propto \exp(\text{PLL}_m)$. We then aggregate these results over all WT sequences in the test set, indexed by $i = 1, \dots, n$, to construct the matrix

$$\langle |z_{\text{MUT}} - z_{\text{WT}}| \rangle_{a \rightarrow b} = \frac{1}{|\mathcal{R}_{a \rightarrow b}|} \sum_{i \in \mathcal{R}_{a \rightarrow b}} \Delta z_i(a \rightarrow b), \quad (\text{S54})$$

where $\mathcal{R}_{a \rightarrow b}$ denotes the WT indices for which $\mathcal{M}(a \rightarrow b)$ is nonempty. For visualization and comparison, we sort substitution types by the dominant left singular mode of $\langle |z_{\text{MUT}} - z_{\text{WT}}| \rangle_{a \rightarrow b}$, which orders WT amino-acid types by the principal pattern of variation in their average mutation-induced displacements.

S. Theoretical sequence descriptors

We constructed a set of 60 theoretical descriptors defined in the IDR literature (listed in Table I) to characterize the compositional and patterning properties of the IDR fragments

studied in this work.

Descriptor	Description
N CPR	Net charge per residue is defined as $\text{N CPR} = \frac{1}{L} \sum_{l=1}^L q_l$, where q_l is the charge of the residue at sequence position l and L is sequence length. Residue charges were assigned according to the Mpipi force field ⁶ , in which R and K carry charges of $+0.75 e$, H carries $+0.35 e$, D and E carry $-0.75 e$, and all other residues are charge-neutral.
FCR	Fraction of charged residues, FCR, of a sequence is defined as its number of charged amino acids divided by its total number of amino acids.
SCD	Sequence charge decoration is defined as $\text{SCD} = \frac{1}{L} \left[\sum_{l=2}^L \sum_{m=1}^{l-1} q_l q_m (l-m)^{1/2} \right]^{15}$, where q_m and q_n denote the charges of residues at sequence positions m and n , respectively, and L is the sequence length.
κ	The parameter κ characterizes the linear sequence distribution of oppositely charged residues ¹⁶ and was computed using localCIDER ¹⁷ . Low and high values of κ correspond to well-mixed and segregated charge distributions, respectively.
$\langle \text{size} \rangle$	In the Mpipi force field, each amino acid is associated with 20 σ parameters that characterize the repulsive core length scales of its nonbonded interactions with each of the 20 amino acid types, including itself (see Sec. I J and Eq. (S46)). For each amino acid, we define $\bar{\sigma}$ as the average of its 20 σ values. The average residue size of a sequence is computed as $\langle \text{size} \rangle = \frac{1}{L} \sum_{l=1}^L \bar{\sigma}_l$, where $\bar{\sigma}_l$ is the $\bar{\sigma}$ of the amino acid at sequence position l and L is sequence length.
$\langle \text{hydrophob.} \rangle$	In the Mpipi force field, each amino acid is associated with 20 ε parameters that scale its nonbonded interaction potential with each of the 20 amino acid types, including itself (see Sec. I J and Eq. (S46)). For each amino acid, we define $\bar{\varepsilon}$ as the average of its 20 ε values. The average residue hydrophobicity is computed as $\langle \text{hydrophob.} \rangle = \frac{1}{L} \sum_{l=1}^L \bar{\varepsilon}_l$, where $\bar{\varepsilon}_l$ is the $\bar{\varepsilon}$ of the amino acid at sequence position l and L is sequence length.
WF_{pairs}	The descriptor WF_{pairs} is the average of the scaled integral of the attractive part of the nonbonded potential over all pairs of residues in a sequence, given by $\text{WF}_{\text{pairs}} = \frac{1}{L(L+1)/2} \sum_{l=1}^L \sum_{m=l+1}^L \int_{\sigma_{lm}}^{3\sigma_{lm}} 4\pi r^2 \phi_{lm}(r) dr$, where σ_{lm} and ϕ_{lm} are the parameters of the nonbonded potential between the residues at sequence positions l and m (see Sec. I J) and L is sequence length.
SHD	Sequence hydrophathy decoration SHD is computed as $\text{SHD} = \frac{1}{L} \sum_{l=1}^L \sum_{m=l+1}^L \varepsilon_{lm} m-l ^{-118}$, where ε_{lm} scales the nonbonded interaction potential between residues at sequence positions l and m and L is sequence length.

Composition descriptors We computed the fractions of residues in the following twelve residue groups to define twelve amino-acid composition descriptors: {G}, {D,E} “negatively charged”, {A,C,I,L,M,P,S,T,V} “neutral”, {N,Q} “neutral with π electron”, {K} “positively charged”, {H,R} “positively charged with π electron”, {F,W,Y} “aromatic”, {K,R}, {K,R,H}, {W}, {F}, and {Y}. The first seven groups are defined in Ref.⁶. The last five groups were included to investigate the distinct roles played by different aromatic and positively charged residues in the Mpipi force field. Each of these composition descriptors is labeled as “Fraction X”, where X is the residue subset (e.g., Fraction DE).

Mpipi composition The twelve composition descriptors described above were concatenated to construct the Mpipi composition descriptor set.

NARDINI descriptors We used NARDINI descriptors to characterize residue patterning for the first nine residue groups defined in the composition descriptors above¹⁹. The Ω descriptor for a residue group X quantifies the binary patterning of residues either belonging to or excluded from the specified group and is labeled as $z(\Omega_X)$ (e.g., $z(\Omega_{DE})$). The δ descriptor for a pair of residue groups X and Y quantifies the binary patterning of residues belonging to the two groups and is labeled as $z(\delta_{X,Y})$ (e.g., $z(\delta_{DE,KR})$). We excluded pairs of groups with overlapping residues in the computation of the δ descriptors, resulting in a total of forty NARDINI descriptors (twelve Ω -family descriptors and twenty-eight δ -family descriptors).

NARDINI The forty NARDINI descriptors described above were concatenated to construct the NARDINI descriptor set.

TABLE I: Theoretical sequence descriptors and descriptor sets used to characterize compositional and patterning properties of IDR sequences.

T. Explained variance and canonical correlation analysis of theoretical descriptors

We analyzed linear relationships between the metric representation and the theoretical descriptors defined in Sec. IS. The feature vectors $z_i \in \mathbb{R}^d$ for IDRs $i = 1, \dots, n$ were stacked to form the matrix $Z \in \mathbb{R}^{n \times d}$. Corresponding D -dimensional theoretical descriptor vectors, denoted $y_i \in \mathbb{R}^D$, were stacked to form the matrix $Y \in \mathbb{R}^{n \times D}$. Because the feature vectors represent coordinates in a metric space with a physically meaningful origin, they were neither centered nor rescaled in these analyses. By contrast, the theoretical descriptors were centered and variance-normalized as described below.

a. Per-descriptor explained variance and metric-space loadings. We first centered and normalized each individual theoretical descriptor $Y_r \in \mathbb{R}$, yielding a whitened scalar descriptor with zero mean and unit variance. We then computed the fraction of the variance of the whitened descriptor Y_r explained by the metric representation Z via a no-intercept ordinary least squares projection onto the span of Z ,

$$R^2(Y_r | Z) = \frac{\|\hat{y}_r\|^2}{\|y_r\|^2}, \quad (\text{S55})$$

where \hat{y}_r denotes the projection of the whitened theoretical descriptor onto the metric space. This quantity measures how well the feature vectors explain variability in each theoretical descriptor. We also computed the descriptor-aligned metric-space loading vector $v_r \in \mathbb{R}^d$. We visualized the squared components v_{rj}^2 , which quantify the contribution of each metric-space dimension j to descriptor r ; the squared components are independent of the sign of the loading and satisfy $\sum_{j=1}^d v_{rj}^2 = 1$.

b. Multivariate explained variance for descriptor subsets and metric-space contributions. To assess how well the metric representation explains collections of multiple theoretical descriptors, we computed a multivariate coefficient of determination $R^2(Y | Z)$ for selected D -dimensional subsets of descriptors. For each selected descriptor subset, we centered and whitened the columns of $Y \in \mathbb{R}^D$ to remove scale and correlation effects. We then projected the whitened descriptor matrix onto the span of Z using no-intercept linear regression and computed the explained variance

$$R^2(Y | Z) = \frac{\text{tr}(\text{Cov}(\hat{Y}))}{\text{tr}(\text{Cov}(Y))}, \quad (\text{S56})$$

where \hat{Y} denotes the projection of the whitened theoretical descriptors onto the metric space. This quantity reports the total fraction of variance of this collection of theoretical descriptors explained by the feature vectors.

For each selected descriptor subset, we used canonical correlation analysis between Z and the whitened descriptor matrix to assess the contribution of each metric-space dimension to the explained variance. We first computed the squared canonical correlations $\{\rho_k^2\}$ and corresponding metric-space canonical loading vectors $\{v_k \in \mathbb{R}^d\}$, where k indexes the canonical modes. We then summarized how strongly each metric-space dimension contributes across all canonical modes by defining a ρ^2 -weighted average of the squared metric-space canonical loading components,

$$\bar{v}_j^2 = \frac{\sum_k \rho_k^2 v_{kj}^2}{\sum_k \rho_k^2}, \quad j = 1, \dots, d. \quad (\text{S57})$$

This quantity measures the overall importance of metric-space dimension j in explaining the variance across selected theoretical descriptors by emphasizing canonical modes with stronger feature vector–descriptor coupling. As in the single-descriptor case, the squared components are independent of the sign of the loading and satisfy $\sum_{j=1}^d \bar{v}_j^2 = 1$.

U. Mutual information analysis

Mutual information between a descriptor (or descriptor set) Y and the metric space representation Z was estimated using the SMILE method²⁰. For each of the 335,439 sequences in our curated IDR fragment ensemble (see Sec. IA), the corresponding value of Y was paired with metric-space representations Z generated by each of the five encoders trained in 5-fold cross-validation (see Sec. IL), resulting in 1,677,195 joint (Y, Z) samples.

The 235,439 training and validation sequences were randomly divided into three partitions for mutual information evaluation. For each fold $k = 1, 2, 3$, two consecutive partitions (k to $k + 1$, cyclically) were used for training, the remaining partition for validation, and the 100,000 held-out test sequences for testing. Mutual information $I(Y, Z)$ was estimated with the joint (Y, Z) data of each fold using the `estimate_mi` function from the `torch_mist`

package²¹, with a patience of 10 epochs, a τ value of 25, and a *critic* neural network consisting of two hidden layers with 256 neurons in each. This procedure produced three test estimates of $I(Y, Z)$, whose average was recorded. The entire process was repeated five times, yielding a total of 5 average test estimates. The mean and standard deviation of these 5 estimates are reported as the value of $I(Y, Z)$ and its uncertainty, respectively.

The entropy of the metric space representation, $H(Z)$, was estimated by computing $I(Z_{\text{avg}}, Z)$ using the same procedure as for $I(Y, Z)$, where Z_{avg} denotes the model-averaged feature vectors obtained from the five transformer encoders trained via 5-fold cross validation. In the `estimate_mi` function, a batch size of 4,096 was used when evaluating $I(Y, Z)$ for all the 60 individual descriptors (except for $z(\delta_{\text{K,FWY}})$) and the descriptor set NARDINI (see Sec. IS), while a batch size of 65,536 was used in all other cases for stability.

V. Counterfactual analyses using mutant fragments

To isolate sequence-dependent effects, we analyzed the thermodynamic consequences of mutations that preserve amino-acid composition. Following the approach described in Sec. IB, we constructed composition-preserving multi-swap and single-swap mutant sequences. We refer to these mutants as counterfactuals, since any change in their metric-space representation relative to the corresponding WT sequence can be attributed to the ordering of the amino acids within the sequence rather than amino-acid identity.

1. EOS test loss for mutant mixtures

We first computed the EOS test loss for mixtures of composition-preserving mutant sequences. We replaced each WT sequence in the uniform-metric-space test set with a multi-swap mutant generated via MCMC sampling (see Sec. IB). We then repeated the EOS simulations using these mutant (MUT) mixtures. We quantified the overall difference between the WT and MUT mixtures by computing the root-mean-square of $(P_{\text{MUT}} - P_{\text{WT}})/c_{\text{tot}}$, where the subscripts indicate whether WT or MUT sequences were used in the simulations. We estimated the error on this quantity by linearly propagating the simulation uncertainty. We then evaluated the test loss, $\text{MSE}((\hat{P} - P)/c_{\text{tot}})$, on the mutant mixtures. As a negative control, we also evaluated the test loss for mislabeled datasets in which we paired the prediction for WT mixtures with simulations of MUT mixtures and vice versa.

2. Analysis of metric effects due to single-swap mutations

Having established that composition-preserving mutations alter the EOS and that the metric representation captures these effects, we next carried out more detailed statistical analyses of metric-space displacements arising from composition-preserving mutations. To ensure sufficient statistical power, we utilized an exhaustive enumeration of all unique single-swap mutants (see Sec. IB). We then analyzed (a) the overall distribution of metric-space distances between these mutants and their respective WT sequences, (b) the position dependence of mutational effects within the sequences, and (c) the influence of short motifs within the WT sequences on these mutational effects. In all cases, we computed weighted averages over all sequences derived from a WT sequence with weights $w_m \propto \exp(\text{PLL}_m)$ and

then aggregated these results over all WT sequences in the 100,000-sequence test set (see Sec. IB).

a. Global distribution of counterfactual spread. For each WT sequence i in the test set, we computed the spread of metric-space distances over the set \mathcal{S}_i consisting of the WT sequence and all associated unique single-swap mutants,

$$\text{Spread}_i = \left\langle \left\| z_m - z_i^{\text{cent}} \right\|_2^2 \right\rangle_i^{1/2}, \quad z_i^{\text{cent}} = \langle z_m \rangle_i, \quad (\text{S58})$$

where $m \in \mathcal{S}_i$ and the averages are PLL-weighted. To summarize counterfactual variability across the test set, we aggregated the spreads associated with all WT sequences into an ensemble-level histogram. We then analyzed typical properties of the WT sequences whose mutants lead to the highest 10% and lowest 10% spreads in the ensemble-level histogram. To this end, we computed histograms of individual whitened theoretical descriptors using WT sequences in either the top-10% or bottom-10% of the spread distribution. We then ranked the relevance of these descriptors for distinguishing these two classes of WT sequences by computing the empirical mutual information between the class label and the pair of histograms for each whitened theoretical descriptor.

b. Position-dependent counterfactual spread. To assess positional dependence, we restricted \mathcal{S}_i to the WT sequence and the subset of unique single-swap mutants whose sequence differs from the WT at position l . For each position $l \in \{1, \dots, L\}$, we computed the corresponding spread $\text{Spread}_{i,l}$ using the same definition as above. We then aggregated these values over WT sequences to obtain the ensemble-level, position-dependent spread

$$\langle \text{Spread}_l \rangle = \frac{1}{|\mathcal{R}_l|} \sum_{i \in \mathcal{R}_l} \text{Spread}_{i,l}, \quad (\text{S59})$$

where \mathcal{R}_l denotes the set of WT sequences for which position l admits at least one single-swap mutant. We similarly defined a position-dependent spread conditioned on the WT amino acid at the swapped position l having type $a \in \mathcal{A}$, $\langle \text{Spread}_{l,a} \rangle$, by further restricting the set \mathcal{S}_i and aggregating the results analogously to Eq. (S59).

c. Motif-level analysis of counterfactual spread. Finally, we analyzed counterfactual effects associated with short sequence motifs defined as ordered tuples of residue classes, $M = (C_1, \dots, C_{L_{\text{motif}}})$, where each wildcard $C_\ell \subset \mathcal{A}$ specifies an allowed set of amino acids and L_{motif} is the motif length. The wildcards utilized in this work are presented in Table II. Motifs are treated as equivalent under reversal, defining a canonical motif class $[M] = \{M, M^{\text{rev}}\}$. A WT sequence is said to satisfy a motif if it contains a contiguous subsequence whose residues match the wildcard classes in M or its reversed counterpart M^{rev} . A corresponding motif-control class is defined by requiring only that the same wildcard classes be satisfiable at distinct positions anywhere in the WT sequence, in any order, without positional contiguity. For a given WT sequence i , we formed the set \mathcal{S}_i consisting of the WT sequence and all unique single-swap mutants that alter at least one WT position participating in a satisfying match of the motif or its control. For each motif and control class, we computed the corresponding spread over \mathcal{S}_i as above and then aggregated these values across WT sequences following the same logic as Eq. (S59).

Wildcard class	Symbol	Amino acids
Positive	+	K, R, H
Negative	-	D, E
Hydrophobic	h	A, F, I, L, M, V, W, Y
Polar	p	C, N, Q, S, T
Any	*	A, C, D, E, F, G, H, I, K, L, M, N, P, Q, R, S, T, V, W, Y

TABLE II. Definitions of amino-acid wildcard classes used in motif specifications.

II. DATA SETS AND COMPUTATIONAL RESOURCES USED

Type of simulation	CPU core-hours per sim.	GPU hours per sim.	Data set name	Number of elements	Total computation resources (CPU core-hours; GPU hours)
EOS	4–12	n/a	EOS_unilat_test_single	10,050	~ 80,400
			EOS_unilat_test_pair	10,440	~ 83,520
			EOS_unilat_test_trip	10,050	~ 80,400
			EOS_unilat_test_quad	10,050	~ 80,400
			EOS_uniseq_test_single	7,200	~ 57,600
			EOS_uniseq_test_pair	7,140	~ 57,120
			EOS_uniseq_test_trip	7,140	~ 57,120
			EOS_uniseq_test_quad	7,140	~ 57,120
			EOS_uniseq_train_pair	100,000	~ 800,000
			EOS_uniseq_train_single	20,000	~ 160,000
FE diff.	320–960 (single component) 640–1,920 (two or more components)	n/a	EOS_uniseq_train_pair_high_conc	20,000	~ 160,000
			FED_unilat_single	63	~ 40,320
			FED_unilat_pair	231	~ 295,680
			FED_unilat_trip	60	~ 76,800
			FED_unilat_quad	60	~ 76,800
Direct-coex.	10,752–13,824	672–864	DC_seen	59	~ 724,992; 45,312
			DC_unseen	58	~ 712,704; 44,544

TABLE III. Summary of computational resources required for EOS, free-energy (FE) difference, and direct-coexistence simulations. EOS data sets whose names contain train/test were used as training and validation or test data, respectively. The FED data sets were used to construct free-energy density difference test data via explicit thermodynamic integration. For both the EOS and FED data sets, the labels unilat/uniseq indicate that the IDR components in the corresponding systems were sampled uniformly from the metric or sequence space, respectively. The DC_seen/DC_unseen datasets were used to evaluate phase diagram predictions for mixtures composed of IDR sequences that were either encountered (seen) or held-out (unseen) during EOS training and validation; in both cases, the test mixtures themselves were not encountered during EOS training and validation.

REFERENCES

- [1] G. Tesei, A. I. Trolle, N. Jonsson, J. Betz, F. E. Knudsen, F. Pesce, K. E. Johansson, and K. Lindorff-Larsen, *Nature* **626**, 897 (2024).
- [2] Z. Lin, H. Akin, R. Rao, B. Hie, Z. Zhu, W. Lu, N. Smetanin, *et al.*, *Science* **379**, 1123 (2023).
- [3] M. Zaheer, S. Kottur, S. Ravanbakhsh, B. Póczos, R. R. Salakhutdinov, and A. J. Smola, in *Adv. Neur. Inf. Proc. Sys.*, Vol. 30 (2017).
- [4] E. Wagstaff, F. B. Fuchs, M. Engelcke, I. Posner, and M. A. Osborne, in *Int. Conf. Mach. Learn.* (2019).
- [5] J. Sethuraman, *Stat. Sin.* **4**, 639 (1994).
- [6] J. A. Joseph, A. Reinhardt, A. Aguirre, P. Y. Chew, K. O. Russell, J. R. Espinosa, A. Garaizar, and R. Collepardo-Guevara, *Nat. Comput. Sci.* **1**, 732 (2021).
- [7] A. P. Thompson, H. M. Aktulga, R. Berger, D. S. Bolintineanu, W. M. Brown, P. S. Crozier, P. J. in 't Veld, A. Kohlmeyer, S. G. Moore, T. D. Nguyen, R. Shan, M. J. Stevens, J. Tranchida, C. Trott, and S. J. Plimpton, *Comp. Phys. Comm.* **271**, 108171 (2022).
- [8] A. Paszke, S. Gross, F. Massa, A. Lerer, J. Bradbury, G. Chanan, T. Killeen, Z. Lin, N. Gimselshein, L. Antiga, *et al.*, in *Adv. Neur. Inf. Proc. Sys.*, Vol. 32 (2019).
- [9] Z. Zhang, in *IWQoS 2018* (IEEE, 2018) pp. 1–2.
- [10] R. H. Colby and M. Rubinstein, *Polymer physics* (Oxford University Press, 2003).
- [11] G. M. Ginell, R. J. Emenecker, J. M. Lotthammer, A. T. Keeley, S. P. Plassmeyer, N. Razo, E. T. Usher, J. F. Pelham, and A. S. Holehouse, *Science* **388**, eadq8381 (2025).
- [12] K. Adachi and K. Kawaguchi, *Phys. Rev. X* **14**, 031011 (2024).
- [13] S. Mao, D. Kuldinow, M. P. Haataja, and A. Košmrlj, *Soft Matter* **15**, 1297 (2019).
- [14] R. Flamary, N. Courty, A. Gramfort, M. Z. Alaya, A. Boisbunon, S. Chambon, L. Chapel, A. Corenflos, K. Fatras, N. Fournier, L. Gautheron, N. T. Gayraud, H. Janati, A. Rakotomamonjy, I. Redko, A. Rolet, A. Schutz, V. Seguy, D. J. Sutherland, R. Tavenard, A. Tong, and T. Vayer, *J. Mach. Learn. Res.* **22**, 1 (2021).
- [15] L. Sawle and K. Ghosh, *J. Chem. Phys.* **143** (2015).
- [16] R. K. Das and R. V. Pappu, *Proc. Natl. Acad. Sci. U.S.A.* **110**, 13392 (2013).
- [17] A. S. Holehouse, R. K. Das, J. N. Ahad, M. O. Richardson, and R. V. Pappu, *Biophys. J.* **112**, 16 (2017).
- [18] W. Zheng, G. Dignon, M. Brown, Y. C. Kim, and J. Mittal, *J. Phys. Chem. Lett.* **11**, 3408 (2020).
- [19] M. C. Cohan, M. K. Shinn, J. M. Lalmansingh, and R. V. Pappu, *J. Mol. Biol.* **434**, 167373 (2022).
- [20] J. Song and S. Ermon, arXiv preprint arXiv:1910.06222 (2019).
- [21] M. Federici, torch-mist: A pytorch mutual information estimation toolkit (2024).

III. SUPPLEMENTAL FIGURES

S1	EOS simulation uncertainties and MLP model training.	27
S2	Test performance on a uniform-sequence-space test set.	28
S3	Comparison of alternative pairwise theories.	29
S4	Binary phase diagrams for random mixtures of seen and unseen sequences. . .	30
S5	Metric spaces under alternative mixture priors.	31
S6	Complete mutual information analysis of theoretical sequence descriptors. . . .	32

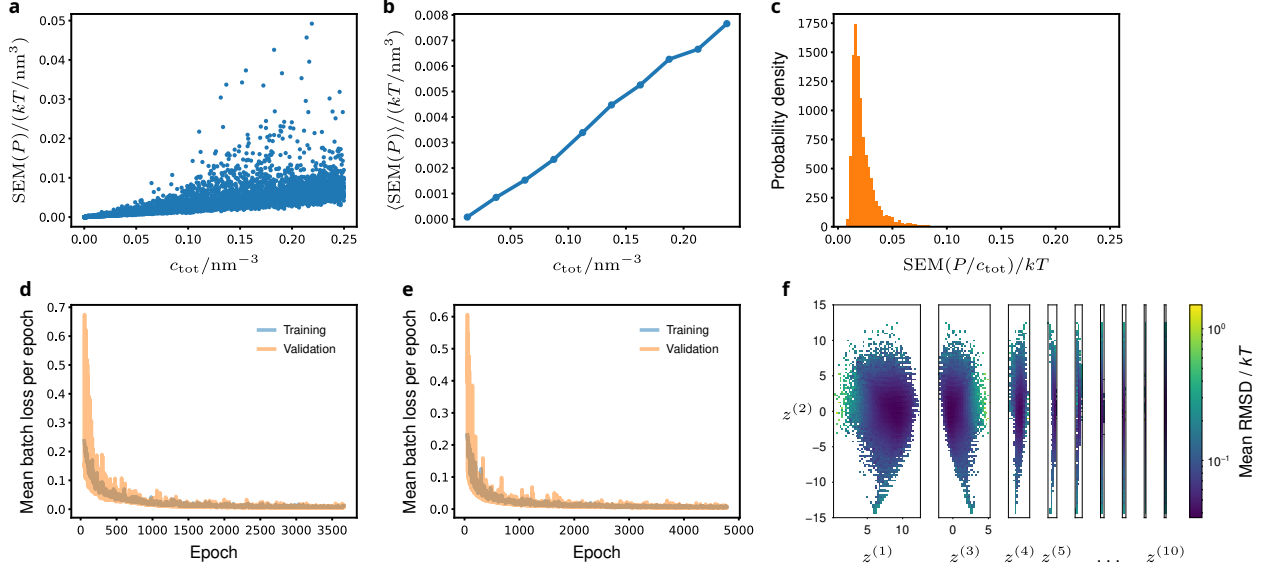


FIG. S1. **Uncertainties in EOS simulations, MLP-model training curves, and metric-space uncertainty.** (a) Standard error of the mean (SEM) of pressure values in the uniform-metric-space EOS test dataset. (b) Mean EOS SEM of the data shown in (a), binned according to the total concentration, c_{tot} . (c) Histogram of the EOS SEM normalized by c_{tot} , demonstrating that the simulation uncertainty on P/c_{tot} is roughly constant across concentrations and mixture compositions. Comparison with the $d = 10$ MLP model loss on this test set (Fig. 1f,g) shows that the model achieves an accuracy within a factor of ~ 3 of the minimum theoretical loss given by $\sim \sqrt{2} \times \langle \text{SEM}(P/c_{\text{tot}}) \rangle$. (d,e) Mean mini-batch loss per epoch for the MLP model with latent dimension $d = 10$ on the training and validation sets. Two example splits from 5-fold cross-validation are shown, each using a randomly selected seed. Loss decreases and stabilizes for both, with minimal evidence of overfitting. (f) Projections of the mean encoder uncertainty across the metric space of the $d = 10$ MLP model (see Fig. 1e).

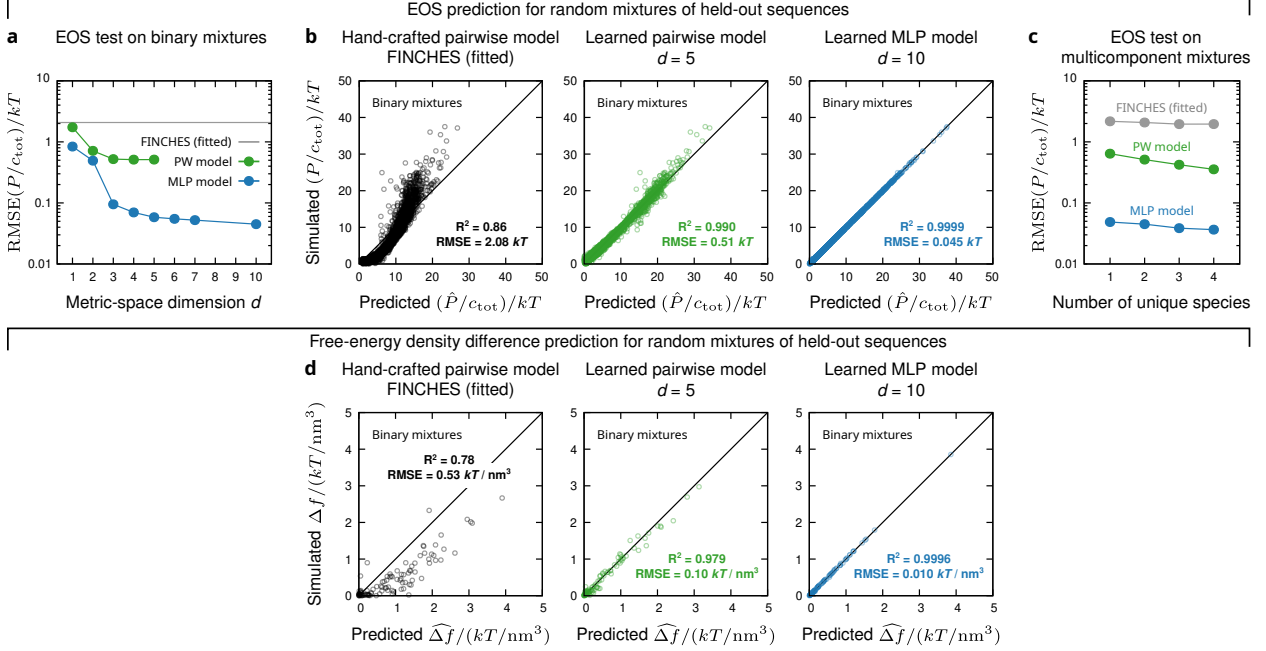


FIG. S2. EOS and free-energy density difference test performance for random mixtures composed of sequences sampled uniformly from the sequence ensemble. All calculations are analogous to those shown in Fig. 1f–k. Overall, test performance tends to be better for the learned models on these datasets relative to the uniform-metric-space datasets presented in Fig. 1f–k, since sequences sampled uniformly from the sequence ensemble tend to be concentrated near the center of the metric-space distribution (see Fig. 1e), where the encoder uncertainty tends to be lowest (see Fig. S1f). (a) EOS test performance evaluated on 7,140 random binary mixtures as a function of the metric-space dimension d . (b) EOS scatter plots for FINCHES, the $d = 5$ learned pairwise model, and the $d = 10$ MLP model, evaluated on random binary mixtures. (c) EOS test performance for the same three models as a function of the number of unique components in a multicomponent mixture. (d) Free-energy density difference test performance evaluated on 100 random binary mixtures for the same three models.

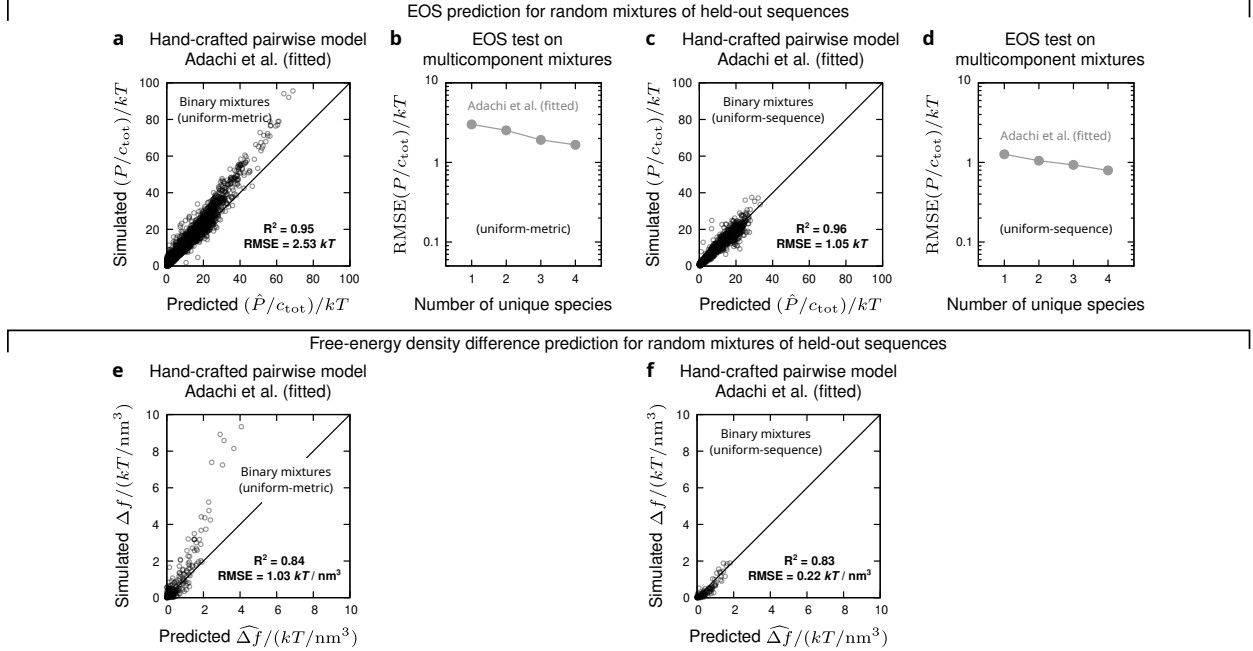


FIG. S3. **Comparison of EOS and free-energy density difference predictions using alternative pairwise theories.** Predictions are shown using the dimer approximation of Adachi et al., with global constants fitted using training and validation EOS data. Overall, the prediction accuracy across all test sets is comparable to the prediction accuracy of FINCHES; however, the relative prediction accuracy of these two hand-crafted models is sensitive to the distribution from which sequences are sampled. (a,b) EOS prediction performance for (a) random binary mixtures and (b) random n -component mixtures composed of sequences drawn uniformly from the $d = 10$ MLP model metric space. (c,d) EOS prediction performance for (c) random binary mixtures and (d) random n -component mixtures composed of sequences drawn uniformly from the sequence ensemble. (e) Free-energy density difference prediction performance for random binary mixtures composed of sequences drawn uniformly from the $d = 10$ MLP model metric space. (f) Free-energy density difference prediction performance for random binary mixtures composed of sequences drawn uniformly from the sequence ensemble.

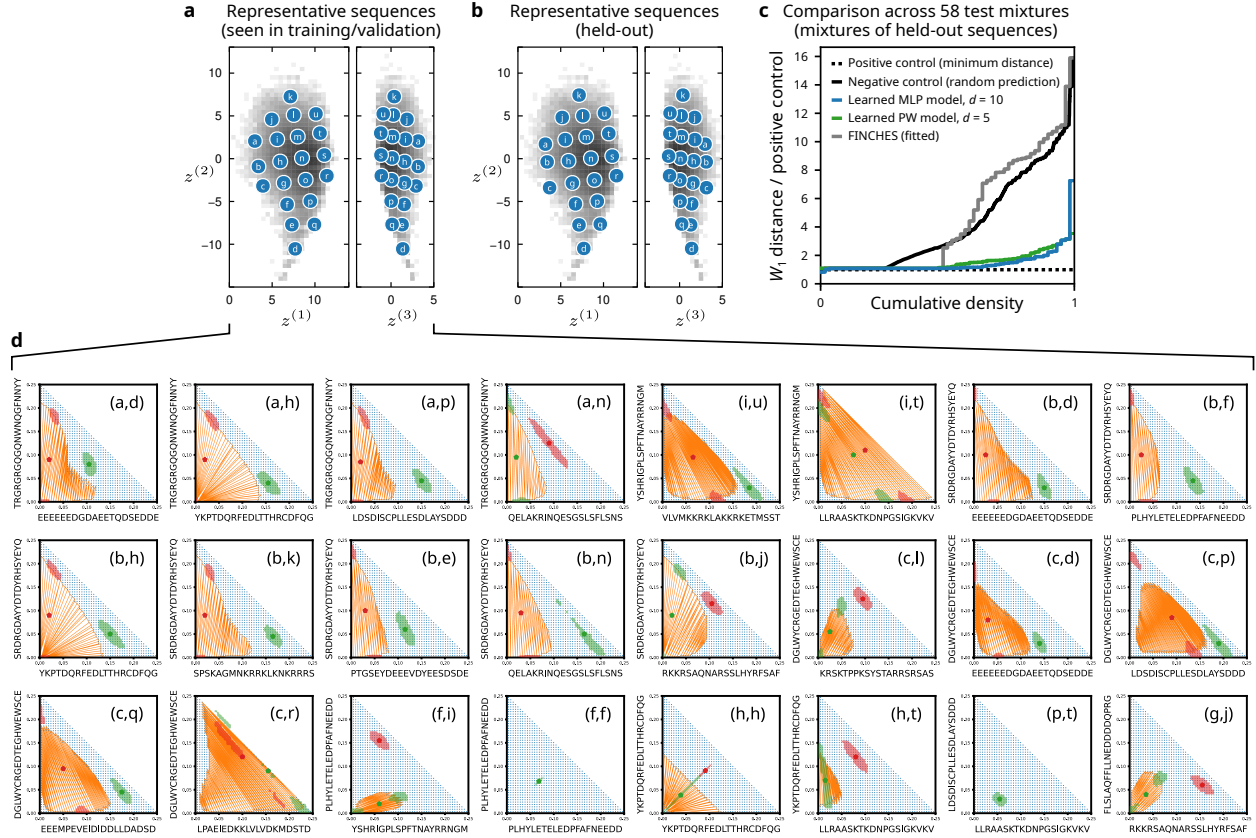


FIG. S4. Comparison of predicted phase diagrams and simulated phase coexistence for random binary mixtures of representative sequences. (a) Representative sequences seen in training and validation, sampled uniformly from the metric space (reproduced from Fig. 2a). (b) Representative held-out sequences, sampled uniformly from the metric space. (c) Comparison of predicted and simulated phase coexistence for random binary mixtures of held-out sequences, following the same format as Fig. 2e. The error in the tail of the cumulative density for the MLP model is due entirely to phase diagrams involving sequence b, which has an anomalously high encoder uncertainty (see Fig. S1f). Otherwise, the predictive performance of the models is similar to that shown in Fig. 2e for mixtures of representative sequences seen in training and validation, which tend to have lower encoder uncertainty. (d) Example predicted binary phase diagrams and simulation comparisons from the test set shown in Fig. 2e. Units and symbols are as in Fig. 2b. Tuples indicate the coordinates of each phase diagram in Fig. 2a. Three-phase coexistence is neither predicted nor observed for binary mixtures of the sequence pairs shown in (a).

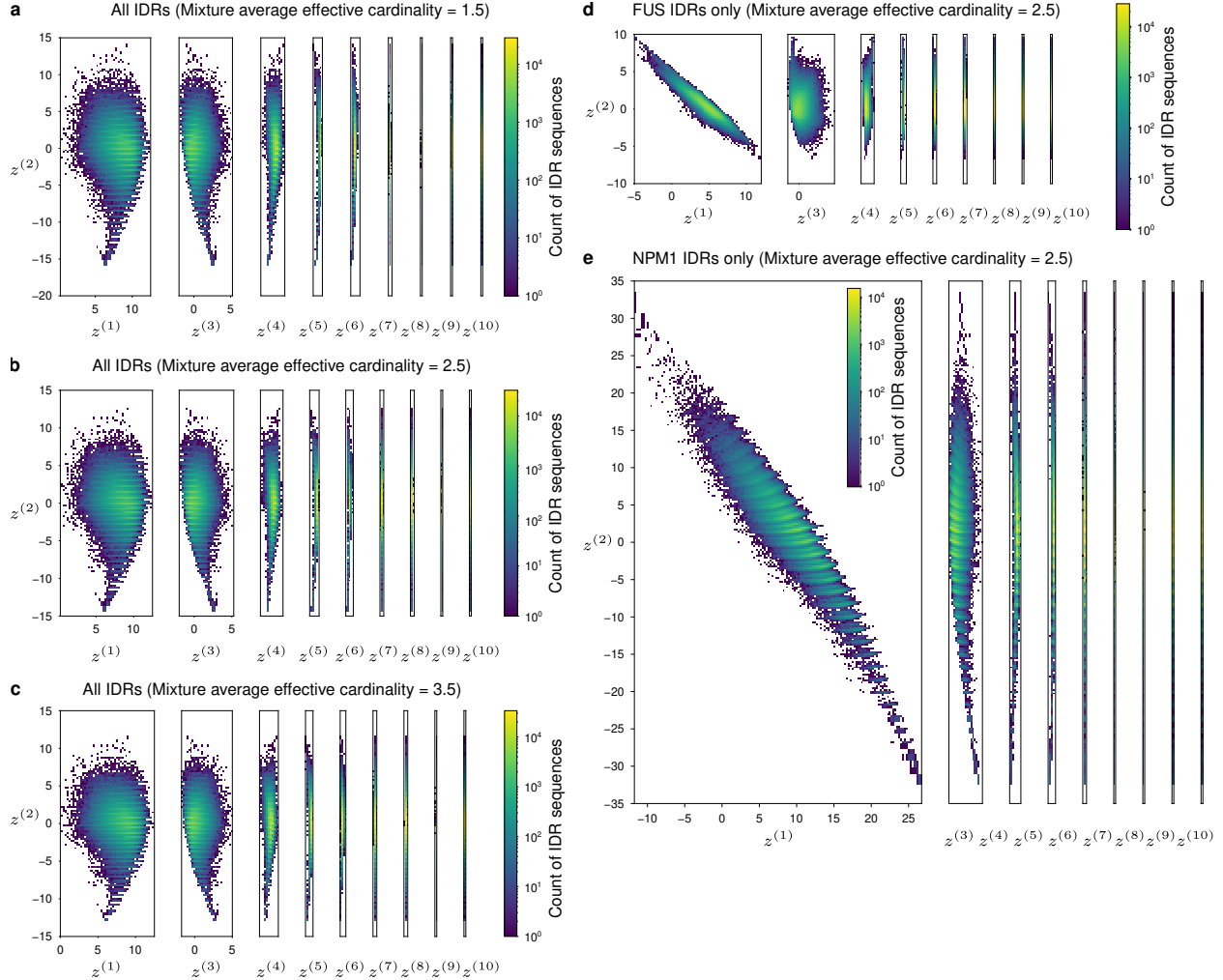


FIG. S5. Distributions of human IDRome sequence fragments under alternative mixture priors. All panels show two-dimensional projections of feature vectors in the $d = 10$ MLP-model metric space under the specified mixture prior, with all distances reported in units of kT . (a,b,c) Metric spaces with mixture priors in which IDRs are sampled uniformly from the sequence ensemble. The Dirichlet distribution sparsity parameter is tuned such that the average effective cardinality (99% mass) across mixtures is (a) 1.5, (b) 2.5, or (c) 3.5. The metric space shown in (b) is used throughout the main text and also shown in Fig. 1e. Increasing the effective cardinality (i.e., reducing mixture sparsity) tends to reduce the spread of the distribution, decreasing thermodynamic distances between IDRs. However, the qualitative properties of these feature-vector distributions remain consistent, indicating that the choice of the sparsity parameter plays a secondary role relative to the choice of the underlying sequence distribution. (d,e) By contrast, changing the sequence distribution from which the mixture prior is composed significantly alters distances between IDRs. Metric spaces with mixture priors in which only (d) FUS fragments or (e) NPM1 fragments are sampled correspond to the context-dependent mutational analyses shown in Fig. 3j,k. These mixture priors both have an average effective cardinality of 2.5. Importantly, changing the mixture prior involves a linear transformation of the metric space and thus does not require model re-training.

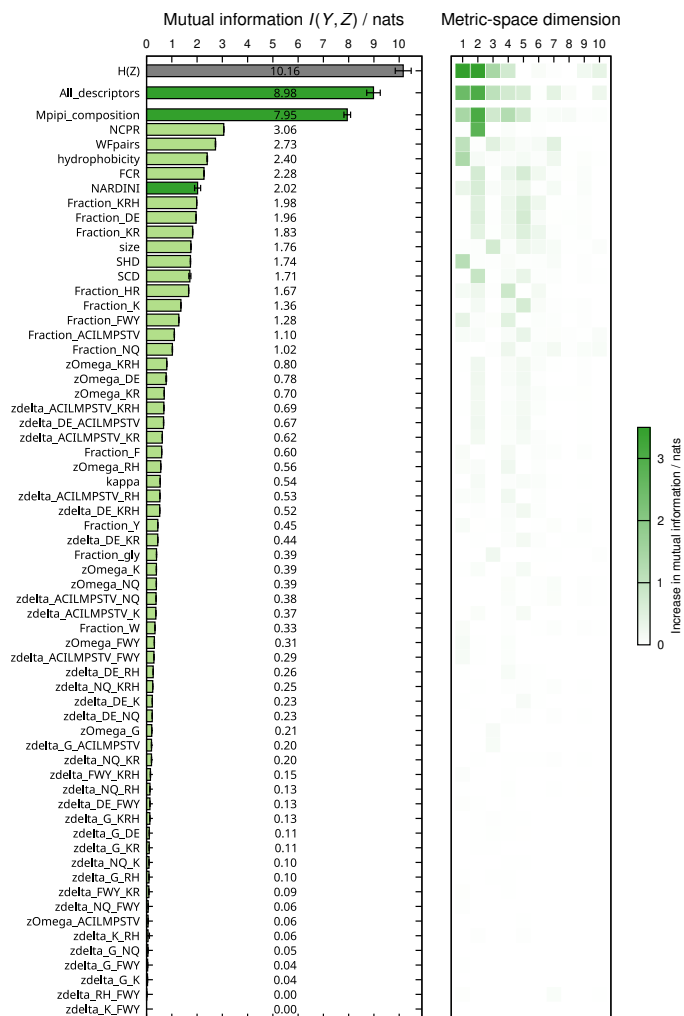


FIG. S6. **Complete mutual information analysis of theoretical sequence descriptors.** *Left:* Mutual information between each individual descriptor (light green) or set of descriptors (dark green) and the $d = 10$ MLP-model metric space. Error bars indicate the standard deviation of five independent estimates. The entropy of the metric space, $H(Z)$, is shown for comparison (gray). *Right:* For each descriptor or descriptor set, the difference between the mutual information relative to the metric space truncated at dimension d and the mutual information relative to the metric space truncated at dimension $d - 1$.